

ISTANBUL TECHNICAL UNIVERSITY ★ GRADUATE SCHOOL OF SCIENCE
ENGINEERING AND TECHNOLOGY

**CLOUD DETECTION AND INFORMATION CLONING TECHNIQUE FOR
MULTI TEMPORAL SATELLITE IMAGES**

Ph.D. THESIS

Kaan KALKAN

Department of Geomatics Engineering

Geomatics Engineering Programme

JANUARY 2017

ISTANBUL TECHNICAL UNIVERSITY ★ GRADUATE SCHOOL OF SCIENCE
ENGINEERING AND TECHNOLOGY

**CLOUD DETECTION AND INFORMATION CLONING TECHNIQUE FOR
MULTI TEMPORAL SATELLITE IMAGES**

Ph.D. THESIS

Kaan KALKAN
(501102609)

Department of Geomatics Engineering

Geomatics Engineering Programme

Thesis Advisor: Prof. Dr. M. Derya MAKTAV

İSTANBUL TEKNİK ÜNİVERSİTESİ ★ FEN BİLİMLERİ ENSTİTÜSÜ

**ÇOK ZAMANLI UYDU GÖRÜNTÜLERİ İÇİN BULUT BELİRLEME VE
KLONLAMA YÖNTEMİ**

DOKTORA TEZİ

**Kaan KALKAN
(501102609)**

Geomatik Mühendisliği Anabilim Dalı

Geomatik Mühendisliği Programı

Tez Danışmanı: Prof. Dr. M. Derya MAKTAV

Kaan Kalkan, a Ph.D. student of İTÜ Graduate School of Science Engineering and Technology 501102609, successfully defended the dissertation entitled “Cloud Detection and Information Cloning Technique for Multi Temporal Satellite Images”, which he prepared after fulfilling the requirements specified in the associated legislations, before the jury whose signatures are below.

Thesis Advisor : **Prof. Dr. M. Derya MAKTAV**
İstanbul Technical University

Jury Members : **Prof. Dr. Filiz SUNAR**
İstanbul Technical University

Prof. Dr. Bülent BAYRAM
Yıldız Technical University

Prof. Dr. Nebiye MUSAOĞLU
İstanbul Technical University

Doc. Dr. Hüseyin TOPAN
Bülent Ecevit University

Date of Submission : 21 December 2016

Date of Defense : 16 January 2017

To peace,

FOREWORD

Clouds are beautiful elements of our photographs and our nature. For satellite images, clouds are important noises for earth observation purposes. This thesis aims to develop a transferable and automated method to detect clouds and shadow from satellite images and clone these features with other multitemporal satellite image dataset to create cloudless mosaics.

This thesis was written after a long study. I would like to give my special thanks to the people who accompanied me on this study.

I would like to express my deepest gratitude my thesis advisor Prof. Dr. Derya Maktav for giving me an opportunity to study with him. This thesis is a results of our long journey of eight years, starting from Roma and GAUS projects to the end of PhD. Special thanks to my dear advisor sharing his knowledge and guidance since the beginning of my Ph.D. study.

I would like to express my deepest gratitude to my thesis committee. Since Prof. Dr. Filiz Sunar is sharing her knowledge and modern vision for any subject we talked for eight years. Dear Prof. Dr. Bülent Bayram was a motivation source and important guide for me while all thesis process.

Finally, I would like to express my deepest gratitude to my wife Berna, my daughter Gamze, my mother, my father, my brother and all my lovely family and friends.

January 2017

Kaan KALKAN
Geomatics Engineer (MSc)

TABLE OF CONTENTS

| | <u>Page</u> |
|--|-------------|
| FOREWORD | ix |
| TABLE OF CONTENTS | xi |
| ABBREVIATIONS | xiii |
| LIST OF TABLES | xv |
| LIST OF FIGURES | xvii |
| SUMMARY | xix |
| ÖZET | xxi |
| 1. INTRODUCTION | 1 |
| 2. BACKGROUND | 5 |
| 2.1 Scientific Approach to Cloudless Mosaic Production..... | 7 |
| 2.2 Cloud Types | 7 |
| 3. DATA AND PRE-PROCESSING | 11 |
| 3.1 Landsat-8..... | 11 |
| 3.1.1 Automatic Download Tool..... | 12 |
| 3.2 Calibration of Data | 13 |
| 3.2.1 Radiance | 14 |
| 3.2.2 Reflectance | 14 |
| 3.2.3 Brightness Temperature | 15 |
| 3.2.4 Atmospheric Correction | 16 |
| 4. CLOUD AND SHADOW DETECTION | 19 |
| 4.1 Segmentation | 20 |
| 4.1.1 SLIC Segmentation | 21 |
| 4.2 Cloud Detection..... | 22 |
| 4.2.1 Classification of Additional Classes (Water and Snow)..... | 22 |
| 4.2.2 Cloud Classification Background (Thermal Band Usage)..... | 23 |
| 4.2.3 Multi-Criteria Cloud Classification Approach..... | 24 |
| 4.3 Shadow Classification | 26 |
| 4.4 Cloud and Cloud Shadow Relation (Cloud Projection Method)..... | 26 |
| 4.5 Results of Cloud and Shadow Detection | 29 |
| 4.6 Accuracy Assessment..... | 30 |
| 5. CLOUD CLONING | 33 |
| 5.1 Choose Best Image to Clone | 36 |
| 5.1.1 Image Correlation Approach..... | 37 |
| 5.1.2 Vector Intersection Approach | 38 |
| 5.2 Edge Smoothing for Seamless and Smooth Cloning | 40 |
| 5.3 Flood Fill for Multitemporal Image Cloning | 40 |
| 5.4 Cloning Results and Image Quality Tests | 41 |
| 6. RESULTS AND DISCUSSION | 45 |
| REFERENCES | 49 |
| CURRICULUM VITAE | 55 |

ABBREVIATIONS

| | |
|-----------------|--|
| ACCA | : Automated Cloud Cover Assessment |
| AWS | : Amazon Web Services |
| BT | : Brightness Temperature |
| COST | : Cosine of the Sun Zenith Angle |
| DN | : Digital Number |
| DOS | : Dark Object Substraction |
| FN | : False Negative |
| FP | : False Positive |
| GUI | : Graphical User Interface |
| HDR | : ENVI Header File |
| ISCCP-FD | : International Satellite Cloud Climatology Project Flux |
| LDCM | : Landsat Data Continuity Mission |
| MCCCD | : Multi Criteria Cloud Cover Detection |
| MTL | : Metadata |
| NASA | : National Aeronautics and Space Administration |
| NDSI | : Normalized Difference Snow Index |
| NDVI | : Normalized Difference Vegetation Index |
| NDWI | : Normalized Difference Water Index |
| NIR | : Near Infrared |
| OBIA | : Object Based Image Analysis |
| OLI | : Operational Land Imager |
| PSNR | : Peak Signal-to-Noise Ratio |
| RGB | : Red Green Blue |
| RMSE | : Root Mean Square Error |
| SLIC | : Simple Linear Iterative Clustering |
| SSIM | : Structural Similarity Index |
| SWIR | : Short Wave Infrared |
| TIRS | : Thermal Infrared Sensor |
| TN | : True Negative |
| ToA | : Top of Atmosphere |
| TP | : True Positive |
| TPR | : True Positive Rate |
| USGS | : United States Geological Survey |
| UTM | : Universal Transverse Mercator |
| VIS | : Visible |
| WGS | : World Geodetic System |

LIST OF TABLES

| | <u>Page</u> |
|--|-------------|
| Table 2.1 : Common cloud types and specifications (CIMSS, 2016). | 7 |
| Table 2.2 : Reflectance characteristics of different surfaces..... | 8 |
| Table 2.3 : Cloud characteristics in visible and infrared images..... | 9 |
| Table 2.4 : Common cloud types from ground photo, infrared and visible satellite images. | 10 |
| Table 3.1 : Technical details about Landsat-8..... | 12 |
| Table 3.2 : Landsat 8-OLI and Thermal Infrared Sensor (TIRS) spectral band characteristics | 12 |
| Table 4.1 : Cloud classification criteria. | 25 |
| Table 4.2 : Shadow classification rules..... | 28 |
| Table 4.3 : Accuracy indicators. | 30 |
| Table 4.4 : Accuracy metrics..... | 31 |

LIST OF FIGURES

| | <u>Page</u> |
|---|-------------|
| Figure 1.1 : General workflow of the study | 4 |
| Figure 2.1 : Global mosaic of cloudless and clear view of Google Maps & Earth..... | 5 |
| Figure 2.2 : Cloudless image generation procedure of Mapbox Co. a) Images of all year b) Normalized c) Cloudless image..... | 6 |
| Figure 2.3 : Common cloud types with reference altitude chart..... | 8 |
| Figure 2.4 : Thin and thick clouds and reflective characteristics..... | 9 |
| Figure 3.1 : Study area and distribution of selected images. | 11 |
| Figure 3.2 : Landsat Path/Row/Date selection and quicklook..... | 13 |
| Figure 3.3 : Landsat study area selection GUI and downloaded image..... | 13 |
| Figure 3.4 : Source of energy, radiance and reflectance | 14 |
| Figure 3.5 : Landsat-8 image radiometric calibration (a) Raw Landsat-8 (b) ToA reflectance calibrated. | 15 |
| Figure 3.6 : Landsat-8 image converted brightness temperature (a) TIR1 (b) TIR2.16 | 16 |
| Figure 3.7 : Landsat-8 image calibration steps (a) RAW Landsat 8 (b) ToA reflectance calibrated (c) DOS 1 Atmospheric corrected. | 18 |
| Figure 4.1 : General workflow chart of study. | 20 |
| Figure 4.2 : Results of SLIC algorithm applied to cloud image (a) Original image (b) SLIC superpixel segmentation result..... | 22 |
| Figure 4.3 : (a) Original RGB image (b) NDWI Index (c) Water classification based on NDWI threshold (LC81910302014163LGN00)..... | 23 |
| Figure 4.4 : (a) Original RGB image (b) NDSI index (c) Snow classification based on NDSI threshold (LC81700322015067LGN00). | 23 |
| Figure 4.5 : Colormap of thermal infrared 2 band (LC81790342014207LGN00). .. | 24 |
| Figure 4.6 : (a) Original RGB image (b) Pixels which are smaller than 300K in TIR2 band (Cloud candidate)..... | 24 |
| Figure 4.7 : Cloud spectral signatures collected from image..... | 25 |
| Figure 4.8 : (a) Original image (b) Cloud detection index (c) Classified cloud areas. | 25 |
| Figure 4.9 : Relationship between clouds and cloud shadow projections. | 26 |
| Figure 4.10 : Cloud and cloud shadow projection relation. | 27 |
| Figure 4.11 : Sun elevation, sun azimuth and zenith angle..... | 27 |
| Figure 4.12 : (a) Original image (b) Shadow detection index (c) Classified cloud shadow areas. | 28 |
| Figure 4.13 : Results of our study compared to Fmask method. | 29 |
| Figure 4.14 : Detailed area from results..... | 30 |
| Figure 4.15 : Graphical descriptions of TP, FP, Precision and Recall..... | 31 |
| Figure 5.1 : Sample result of cloud and cloud shadow detection | 33 |
| Figure 5.2 : Multitemporal dataset..... | 35 |
| Figure 5.3 : Workflow of cloning procedure. | 35 |

| | |
|--|-----------|
| Figure 5.4 : Flowchart of cloud cloning method. Our proposed method consists of six step, superpixel segmentation, cloud detection, algorithm to choose best image to clone (quality assessment), and information reconstruction (cloning)..... | 36 |
| Figure 5.5 : Correlation calculations between images to choose best image to clone. | 37 |
| Figure 5.6 : Finding best cloudless image for cloud patches. | 38 |
| Figure 5.7 : Intersection check between cloud patches. | 39 |
| Figure 5.8 : Intersection percentages of cloud patches with cloud patches in multitemporal image dataset. | 39 |
| Figure 5.9 : Visual intersection rates of cloud patches. | 39 |
| Figure 5.10 : Averaging filter..... | 40 |
| Figure 5.11 : Edges of cloud patches which are applied edge smoothing with averaging filter. | 40 |
| Figure 5.12 : Cloning results after information reconstruction by using Flood Fill method. | 41 |
| Figure 5.13 : SSIM & RMSE results a) Original b) Histogram equalized c) Contrast adjusted d) Salt & Pepper effect e) Blurred f) JPEG converted. | 42 |
| Figure 5.14 : SSIM results and similarity maps of two different cloning results. | 42 |

CLOUD DETECTION AND INFORMATION CLONING TECHNIQUE FOR MULTI TEMPORAL SATELLITE IMAGES

SUMMARY

One of the main sources of noises in remote sensing satellite images are regional clouds and shadows of these clouds caused by atmospheric conditions. In many studies, these clouds and shadows are masked with multitemporal images taken from the same area to decrease effects of misclassification and deficiency in different image processing techniques, such as change detection and NDVI calculation. This problem is surpassed in many studies by mosaicking with different images obtained from different acquisition dates of the same region. The main step of all these studies that cover cloud cloning or cloud detection is the detection of clouds from a satellite image. In this study, clouds and shadow patches are classified by using a spectral feature based rule set created after segmentation process of Landsat 8 image. Not only spectral characteristics but also structural parameters like pattern, area and dimension are used to detect clouds and shadows. Information of cloud projection is used to strengthen cloud shadow classification. Rule set of classification is developed within a transferable approach to reach a scene independent solution. Results are tested with different satellite images from different areas to test transferability and compared to other state-of art methods in the literature. Detection of clouds and cloud shadows features correctly is the main step of cloning procedure to create cloudless image from multitemporal image dataset. Multitemporal image dataset is used to find best image to clone cloud image. Choosing best image for cloning process is an important step for reliable cloning. Statistical and seasonal similarity tests are used to find best image to clone cloud covered image. Vector intersections are used to find cloudless images between multitemporal dataset. Flood Fill method is used to create cloudless image from cloud covered image by using information extraction from cloudless images in dataset. Accuracy of cloning process is tested by using SSIM index to find structural and spectral similarity to cloudless image. All cloning results are tested with different image from different regions to check transferability of study. This study can be regarded as a scientific approach to create cloudless image mosaics for each kind of application. Method in this thesis is a scientific approach to well-known methods of famous cloudless mosaic generation methods of Google, Mapbox Co. etc. for creation of visually good-looking base maps for web maps.

ÇOK ZAMANLI UYDU GÖRÜNTÜLERİ İÇİN BULUT BELİRLEME VE KLONLAMA YÖNTEMİ

ÖZET

Uzaktan algılanmış uydu görüntülerinde atmosfer etkilerinden kaynaklı olarak ortaya çıkan bölgesel bulutlar ve bu bulutların gölgeleri, yapılan çalışmalarda problem oluşturan temel gürültü kaynaklarından. Değişim analizi, NDVI hesaplama gibi önemli dijital işlemlerde bulut ve gölge bölgeleri, genel olarak yanıltıcı sonuçlar veren bölgeler olduğundan dijital işlemler çoğu zaman bu alanlar maskelenerek gerçekleştirilmektedir. Bu problem birçok çalışmada aynı bölgeden farklı zamanlarda elde edilmiş uydu görüntüleri ile mozaikleme yapılarak aşılmıştır. Ancak, mozaikleme sırasında oluşan spektral ve dokusal bozulmalar çalışmaları olumsuz etkilemektedir. Görüntünün çekilme anına bir daha dönülemeyeceğinden, bulutsuz bir görüntü elde etmek önemli bir süreç haline gelmektedir. Google Earth gibi sık kullanılan harita araçları aynı bölgeye ait çekilmiş birçok görüntü kullanarak bu görüntülerin ortalamalarından bulutsuz mozaikler elde ederek kullanıcılara sunmaktadır. Bu çalışmada bulutlu görüntüler çok zamanlı bulutsuz görüntülerden klonlama yapılarak bulutsuz hale getirilecektir. Diğer benzer çalışmalara ek olarak, klonlama süreci bir fotoğraf düzenleme işleminden öte görüntünün spektral özellikleri kullanılarak gerçekleştirilerek en yakın tarih ve spektral benzerlik göz önünde bulundurularak bulutsuz görüntü elde edilecektir. Üretilen bulutsuz görüntüde oluşan kenar bozulma etkileri çeşitli filtreler ile azaltılacaktır.

Geliştirilen yöntem farklı zamanlarda çekilmiş Landsat-8 uydu görüntüleri ile test edilmiştir. Görüntüde bulunan bulutların belirlenmesi, bulut klonlama işleminin gerçekleştirilmesi için ilk aşama ve doğruluğu direkt olarak klonlama doğruluğu etkileyen bir süreçtir. Bulutların oluşturduğu parlaklık ve gölgelerinin oluşturduğu kararmalar birçok veri analizini olumsuz etkilemektedir. Bu etkiler, atmosferik düzeltmede oluşacak zorluklar, NDVI değerlerinin yükselmesi, sınıflandırmadaki hatalar ve değişim analizinin yanlış gerçekleştirilmesi şeklinde olabilir. Tüm bu etkilerin doğrultusunda, uzaktan algılama görüntülerinde bulutlar ve gölgeleri önemli bir gürültü kaynağı olduğundan bunların dijital işlemlerden önceki ilk aşamada belirlenmesi önem taşımaktadır. Bu çalışmada, Landsat-8 görüntüleri kullanılarak ve mevcut ısı bantlarının da yardımıyla, bulut ve gölgelerinin belirlenmesi için bölütleme tabanlı bir kural dizisi ile uygulanan bir yöntem önerilmiş ve test edilmiştir. Çalışmaya temel olan bulut belirleme algoritması, ACCA ve Fmask algoritmalarının geliştirilmiş, sadeleştirilmiş, otomatize edilmiş ve bölütleme tabanlı uyarlanmış bir sürümü olarak değerlendirilebilir. Bu yöntem sayesinde, spektral özellikler ve geometrik özellikler bir arada kullanılarak Landsat 8 görüntülerinden bulut ve bulut gölgeleri belirlenmiştir. Spektral ve geometrik özelliklerin yanı sıra Landsat ısı bant verileri ile, bulut-gölge ve soğuk yüzey (kar, buz) ayırımı güçlendirilmiştir. Komşuluk ilişkileri kullanılarak, belirlenen bulut alanları etrafındaki bulut gölgelerinin belirleme doğruluğu artırılmıştır. Geliştirilen algoritma, dört farklı bölge için farklı zamanlarda çekilmiş Landsat görüntüleri üzerinde test edilerek değerlendirilmiştir.

Bulut belirleme algoritmasında temel olarak Landsat 8 görüntülerinin OLI ve ısı bantları kullanılmaktadır. Landsat-8 verileri, DN değerler olarak işlenmemiş halde sağlanmaktadır. Bu veriler, Landsat verileri ile birlikte gelen meta veri dosyasında (MTL) verilen oranlama katsayıları ile atmosfer üstü yansıtım değerlerine ve radyans değerlerine dönüştürülebilmektedir. Böylece veriler fiziksel anlamı olan birimlere dönüştürülmüş olur. Meta veri dosyasında sağlanan ısı bant katsayıları ile ısı bant verileri, parlaklık sıcaklığı bilgisine dönüştürülebilmektedir. OLI bantları atmosfer üstü yansıtım değerlerine (ToA), ısı bantları ise parlaklık sıcaklığına dönüştürülerek algoritmada kullanılmıştır. Yansıtım değerlerine dönüştürülen görüntülerde bulut alanlarının belirlenmesi için öncelikle bölütleme algoritması ile görüntü süper-piksellelere ayrılmış ve kural tabanlı bir sınıflandırma dizisi uygulanarak bulut alanları görüntü üzerinden belirlenmiştir. Bulut alanlarının belirlenmesinden sonra, spektral testler ve bulut alanlarının komşuluk ilişkileri değerlendirilerek bulut gölgesi alanları da belirlenmiştir.

Süper pikseller, pikselleri anlamlı gruplar halinde birleştirerek, piksel grupları oluşturmak için kullanılmaktadır. Görüntüdeki aynı bilgiye sahip olan piksellerin birleştirilmesi ile görüntü işleme amaçlı işlemlerin hızı da yüksek oranda artmaktadır. K-ortalama (K-means) yönteminin mekânsal özelliklerini de kullanan bir uyarlamasını temel alarak süper pikselleri üreten SLIC algoritması da bu amaçla kullanılan etkin yöntemlerden biridir. Bulut süper piksellerinin üretilmesinde SLIC yöntemi kullanılmıştır.

Görüntülerden bulut alanlarının belirlenmesi için, bulutların spektral karakteristiğinin belirlenmesi ile işleme başlanmıştır. Görüntü üzerinden toplanan bulut noktalarının spektral imzaları karşılaştırılmıştır. Algoritma bu imzalar temel alınarak geliştirilmiştir. Bulut özelliklerine benzer şekilde, bulut gölgesi alanlarının sınıflandırılmasında da, görüntü üzerinden toplanan bulut noktalarının spektral imzalarının yorumlanmasını temel alan bir yöntem ile ısı bantı devre dışı bırakan bir bant oranlama indeksi geliştirilmiştir. Bu indeks ile gölge alanlarının değeri diğer arazi örtüsü özelliklerinden keskin bir şekilde ayrıldığından eşik değeri belirlenmesi dinamik olarak gerçekleştirilebilmektedir. İkinci olarak, farklı gölge alanlarının, bulut gölgeleri ile karışmasını önlemek amacıyla görüntü özniteliklerinden olan güneş azimut açısı kullanılarak tüm bulut bölgelerinin bu açı ile doğru orantılı şekilde belli bir uzaklıkta izdüşümü alınmıştır. Bu izdüşüm alanları, potansiyel gölge alanlarını ifade etmektedir. Gölge alan belirleme indeksi sonucu ile bu izdüşüm alanlarının kesişimi final gölge bölgelerinin sınıflandırılmasında kullanılmıştır.

Bulut ve gölgelerinin belirlenmesi, uzaktan algılamada uzun zamandır üzerinde çalışılan ve birçok yöntemin geliştirildiği bir konudur. Bu yöntemler kimi zaman yeterli doğrulukta sonuçlar verirken, kimi zaman da yeterli doğruluğu sağlayamamaktadır. Piksel tabanlı yöntemlerin yanı sıra, görüntüyü süper-piksellelere ayıran bölütleme tabanlı yöntemlerin bulut ve gölge belirlemede kullanılması yeni bir konudur. Bu şekilde, görüntü, homojen özellikler sergileyen piksel gruplarına ayrılarak, hem hesaplama gücü azaltılmakta, hem de nesne tabanlı bir yaklaşım sergilendiğinden, sınıflandırılması hedeflenen özellikler geometrik karakteristikleri bakımından etkin bir şekilde görüntü üzerinden elde edilebilmektedir. Bu çalışmada geliştirilen bulut ve gölge belirleme algoritmaları ile bölütleme tabanlı bir yaklaşım bu kapsamda uygulanmıştır. İlk aşamada elde edilen süper-piksellerin doğruluğu sınıflandırma doğruluğunu doğrudan etkilemektedir. Bu nedenle küçük bir ölçek parametresi seçilerek süper-piksellerin boyutları küçük tutulmuş ve piksel gruplamaları homojen tutularak, heterojen süper-piksellerin oluşması olasılığı

azaltılmıştır. Bulut ve gölge gibi nesnelere, parlak ve koyu yansıtım değerleri nedeniyle görüntü üzerindeki spektral karakteristikleri belirgin bir şekilde oluşan özelliklerdir. Bu bilgiler esas alınarak SLIC algoritması ile etkin bir bölütleme uygulanarak bulut ve gölge alanları süper-piksellere ayrılmıştır. Spektral tabanlı bir yaklaşımla geliştirilen indeksler ile kural seti şeklinde bir yapı kurularak; parlaklık sıcaklığı, güneş açısı, NDSI, NDWI gibi özellikler de sınıflandırma kural setine eklenerek, çok kriterli bir yapıda bulut ve gölge alanları görüntü üzerinden belirlenmiştir. Burada yeni bir yaklaşım olan bulut-gölge izdüşümü yaklaşımı ile bulut ve gölge arasındaki geometrik bağıntı kullanılarak gölge sınıflandırması doğruluğu artırılmıştır. Tüm bu sonuçlar farklı bölgelerden alınmış görüntüler üzerindeki aynı parametreler ile koşturularak, yöntemin transfer edilebilirliği test edilmiştir. ACCA, Fmask gibi algoritmaların yanında, burada geliştirilen algoritma, transfer edilebilirliği, süper-piksel tabanlı olması sebebiyle getirdiği işlem kolaylığı ve basitleştirilmiş işlem adımları ile kullanılabilirliğini kanıtlamıştır.

Bulut ve gölge alanlarının tespitinden sonra klonlama işlemine altlık oluşturacak bulut maskeleri elde edilmiştir. Bulut alanlarının, bulutsuz görüntülerden hangisi seçilerek klonlanmasına görüntüler arasında yapılan spektral benzerlik testleri ile karar verilmiştir. Tüm bu görüntülerin bulutlu görüntüye olan korelasyonları hesaplanarak korelasyonu en yüksek olan görüntü bilgi aktarımı için kullanılmıştır. Görüntülerin klonlanmasında, bulutlu görüntünün çekildiği tarihe en yakın 3 aylık görüntüler girdi olarak alınmıştır. Tespit edilen bulut alanları ayrı ayrı analiz edilerek, öncelikle seçilen alana yakın tarihli görüntülerde aynı bölgenin bulutsuz olup olmadığı görüntülerin keşifimleri alınarak test edilmiştir. Bu testin sonrasında bulutsuz görüntüler ile bulutlu görüntü arasında korelasyonu en yüksek görüntüden taşıma algoritması ile (Flood Fill) bilgi aktarımı yapılarak bulutsuz görüntü elde edilmiştir.

Görüntülerin klonlanmasından sonra oluşan kenar bozulma etkilerinin düzeltilmesi için, klonlanan bölge sınırlarına ortalama filtresi (mean filter, averaging filter) uygulanmıştır. Görüntülerin klonlanmasının ardından, üretilen bulutsuz görüntülerin yakın zaman ait bulutsuz görüntülere olan benzerliği, Yapısal Benzerlik İndeksi Yöntemi (YBIY) (Structural Similarity Index) ile test edilmiştir. YBIY iki resim arasındaki benzerliğin ölçülmesi için geliştirilmiş, Karesele Ortalama Hata'nın (KOH) geliştirilmiş bir sürümü olan ve sık kullanılan bir yöntemdir. Bu yöntem, karşılaştırılan görüntülerden birisini mutlak doğru olarak kabul ederek, diğer görüntünün bu görüntüden sapmasını tespit etmektedir. Görüntünün kontrast ve spektral özelliklerini yanı sıra, yapısal bozulmalarını da hesaplamaya kattığından çalışma için uygun yöntem olarak belirlenmiş ve uygulanmıştır.

Bulutlu görüntülerdeki bulutların giderilmesi uzaktan algılama disiplini üzerinde çalışanların uzun zamandır çalıştığı bir konudur. Sis etkisinin giderilmesi için bazı spektral yöntemler geliştirilmiş olsa da, geçirimsiz bulutların giderilmesi ancak farklı zamanlı uydu görüntülerinden bilgi aktarımı ile gerçekleşmektedir. Bu çalışmada, yapılan diğer çalışmalarda kazanılan bulut belirleme başarımının sonrasında bu bilgi kullanılarak görüntüde bulunan bulutların, aynı bölgeden çekilmiş farklı zamanlı görüntülerden bilgi aktarımı ile bulutsuz hale getirilmesi sağlanmıştır. Diğer bulutsuz görüntü elde etme yöntemlerinin yanı sıra, bulutlu alanların bulutsuz görüntülerden klonlanması sırasında, görüntülerin spektral ve yapısal özelliklerini korumak ön planda tutulmuştur. Farklı görüntü benzerlik ve görüntü kalitesi yöntemleri kullanılarak sadece görsellik önde tutulmadan spektral ve yapısal bilgiyi de koruyan bir yöntem geliştirilmiştir.

1. INTRODUCTION

One of the main problems of optical remote sensing is clouds and cloud shadows by atmospheric conditions during data acquisition. Shadows and bright features caused by clouds are affecting data analysis processes. These effects are; rising NDVI values, misclassification results and difficulties for atmospheric correction (Zhu et al, 2012). In remotely sensed images, clouds and shadows are vital parts of noises and detection of these features are crucial for further digital image processing analysis (Arvidson et al, 2001; Irish, 2000). Clouds are becoming vital problem for classification and image interpretation processes when there is no chance to acquire new cloudless images (Zhang et al, 2010).

Elimination of haze effects and information reconstruction from multitemporal satellite images are the main methods to produce cloudless images. Tools like Google Earth, are producing cloudless mosaics by using multitemporal images of the same region by averaging them (Hancher, 2016).

Averaging multitemporal images is giving better visual appearance for usage such as base maps but not a scientific approach to produce cloudless scenes. In this study, cloudless images are created by cloning cloudless regions from multitemporal dataset. Furthermore, in a addition to other works, spectral features and seasonal effects are considered to create cloudless image. Edge effects are also smoothed by using different edge smoothing filters.

Cloud detection algorithms are mainly grouped into two categories; classification based algorithms and rule-set based algorithms (Huang et al, 2010). Classification based methods use training sets to classify cloud features similar to traditional classification approach (Simpson et al, 1995; Amato et al, 2008). Rule-set based algorithms need pre-defined cloud specific features for implementation. Automation of these processes is quite difficult to implement because of difficulties in characterization of cloud features. ACCA (Automated Cloud Cover Assessment) method which is developed by Irish in 2006 is an example of an automatic cloud cover

detection algorithm for Landsat 7 images (Irish et al, 2006). ACCA method is considered as a fundamental method for classification of cloud features in Landsat images (Irish, 2000; Saunders et al, 1988). The aim of this algorithm is detection of cloud ratio in the scene and appending this information to image metadata as "cloud cover". ACCA algorithm uses different spectral filters and thermal infrared channels for detection of clouds. Nevertheless, cloud and shadow boundaries are not precisely determined for automated analysis of multitemporal Landsat images in this algorithm (Zhu and Woodcock, 2012). ACCA fails to be precise about detection of warm cirrus clouds and detects snow and ice as clouds in high-latitude regions. (Irish, 2000; Saunders et al, 1988). Another most-used cloud and shadow detection algorithm is Fmask method. Fmask is an object-based cloud and cloud shadow detection method for Landsat images. Fmask uses Top of Atmosphere (ToA) reflectance and Brightness Temperature (BT) to find potential cloud pixels, then uses object-based cloud and cloud shadow matching process to find cloud shadows precisely.

Beyond understanding cloud detection algorithms, visual characterizations of clouds are important to solve this problem. Clouds in satellite images are visually categorized into two groups; opaque clouds and semi-transparent clouds. Determination of opaque clouds are easier to identify because of their high brightness features in visible channels. Since, their signal covers both clouds and surface underneath cloud features, identification of semi-transparent clouds is difficult (Gao et al, 1995, 1998, 2002). Cloud and shadow detection seems as a state-of-art task according to characteristics of clouds' bright behaviour and dark features of their shadows. In contrary, other possibilities can occur in different images such as clouds which are not bright and cold and shadow which are not dark. Also, shadows of clouds over land can occur in many different ways. Based on these anomalies, shadow detection process is quite harder than cloud detection. Mostly, cloud region detection studies are completed by spectral tests. Spectral test can detect shadows in some conditions, but shadows caused by topography, wet areas, dark surfaces, and shadows which don't cause sufficient amount of darkness and cannot be detected only by spectral methods (Saunders and Kriebel, 1998; Hutchison, 2009). Recently geometry based cloud shadow detection methods have been studied and shown to be more successful. Cloud shadows and clouds are matched by each other in object matching method which is well-known and

tested method in geometry based methods (Le Hégarat-Masclé and Andre, 2009; Berendes et al, 1992; Simpson et al, 1998, 2000)

In the light of all informations given above, cloud and shadow detection procedure is an ongoing work in remote sensing. In this study, a new method is proposed which is inspired by all methods mentioned in this paper about cloud and cloud shadow detection. Our proposed method detects clouds and cloud shadows from Landsat 8 images by using both spectral and geometrical properties after a superpixel segmentation process. Beside spectral and geometric properties, discrimination of cold surface (snow, ice) and cloud-shadow relation is strengthened by using thermal infrared channels of Landsat. Neighbourhood relations are used to improve detection accuracy of cloud shadow regions around cloud areas. This method is tested with four different Landsat images taken from different study areas at different acquisition dates. This study can be regarded as a simplified, modified, automated and segmentation based version of ACCA and Fmask methods (Saunders and Kriebel, 1998; Zhu and Woodcock, 2012).

Information reconstruction concept applied to cloud satellite images gives sufficient results for creating cloudless images from multitemporal image dataset. Cloning cloud patches from cloudless multitemporal dataset is the information reconstruction concept of this study. Superpixel segmentation detects cloud patches accurately to start Flood Fill process to reconstruct cloudless information for cloud patches. Choosing best image for cloning process is an important step to conserve spectral consistency. Patch by patch correlation calculations between multitemporal dataset are used to find best image for cloning in terms of spectral consistency. Vector intersection calculations are also used to find best cloudless dataset for cloning process to achieve full cloudless patch cloning. Information reconstruction from cloudless image to cloud image is implemented by using Flood Fill algorithm by pixel-by-pixel which is one of the most known graphical filling algorithm used in graphical applications. Conservation of spectral and structural consistency is the main aim of our proposed cloning algorithm. SSIM is used to evaluate accuracy of cloning in terms of spectral and structural consistency with cloudless reference image. Transferability of proposed method is also tested by using different satellite images from different study areas by using satellite images with different acquisition dates. Accurate detection of cloud and shadow patches for cloning process is most important step. Information reconstruction for

cloud images by our proposed method gives sufficient results for passive remote sensing applications which are interrupted by clouds. Method developed within this study can yield continuity for analyses such as time series and NDVI calculations.

Cloud covers, which are generally present in optical remote sensing images, limit the usage of acquired images and increase the difficulty in data analysis. Thus, information reconstruction of cloud covered images generally plays an important role in image analysis. This thesis proposes a novel method to reconstruct cloud and cloud shadow information in multitemporal remote sensing images. Based on the concept of utilizing spectro-temporal relationships, we propose a superpixel based information reconstruction algorithm that segments images into superpixels containing clouds and cloud shadows and then clones information from cloud-free and high-similarity patches to their corresponding cloud patches.

Workflow of the study is given in Figure 1.1 in detail.

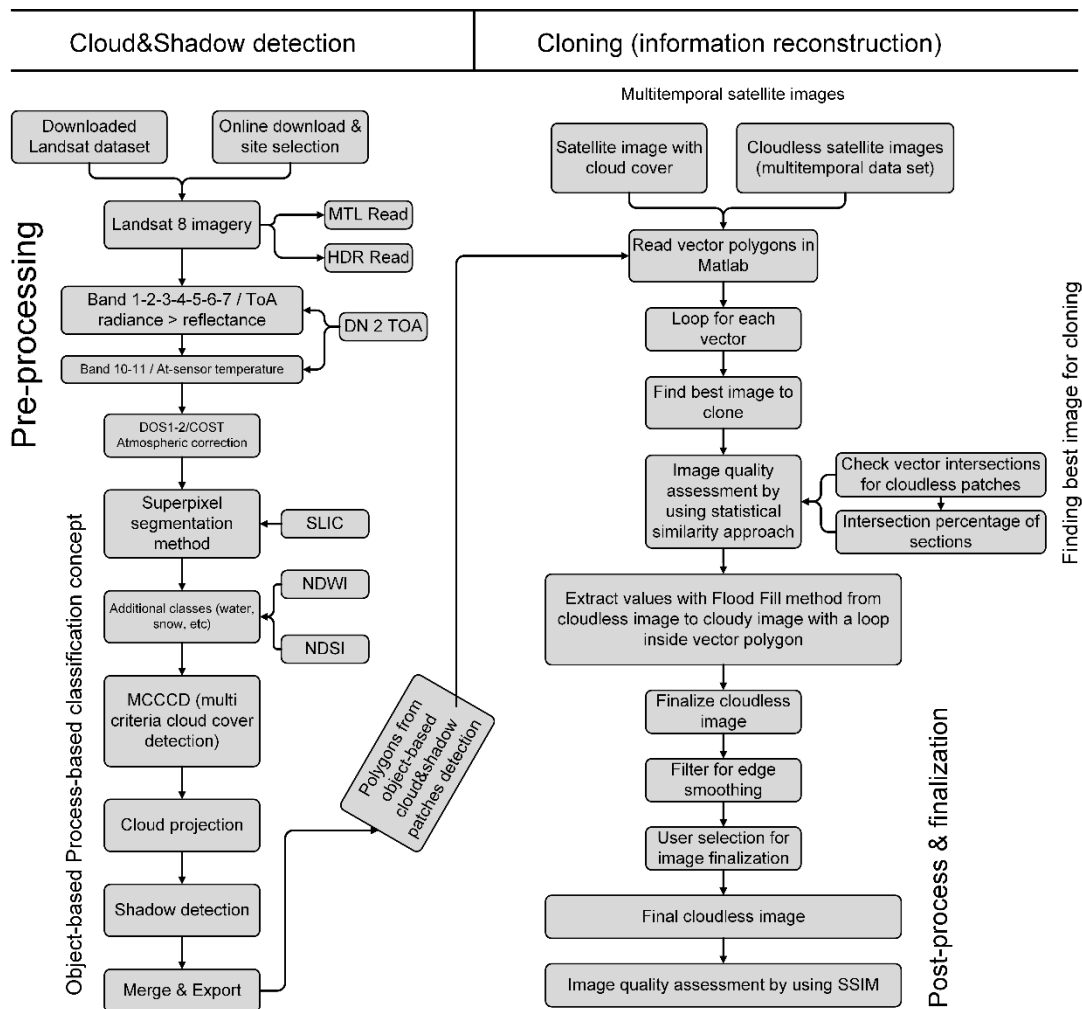


Figure 1.1 : General workflow of the study

2. BACKGROUND

Companies such as Google and Mapbox are using satellite images base maps for their web maps (Gundersen, 2013; Hancher, 2016). Cloudless mosaics are important for showing to users their interested area cloudless and updated (Figure 2.1, Figure 2.2).

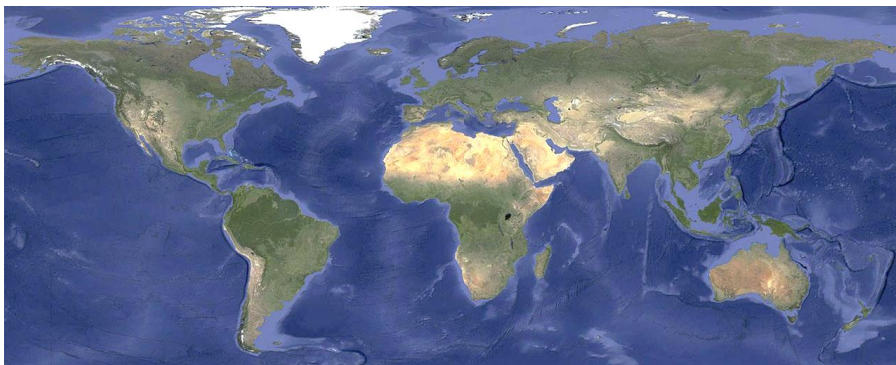


Figure 2.1 : Global mosaic of cloudless and clear view of Google Maps & Earth

Landsat satellite images are commonly used for small scale cloudless base map mosaic creation. Aqua and Terra satellite images are also used for global scale base maps. Detection and elimination of clouds and shadow patches is important for analysis of satellite images for different applications such as creation of cloudless base maps. These maps are used by millions of people in a day. When a user searched an area to check satellite image in Google Earth, it is important to show cloudless and updated image to users which makes cloudless image production more important.

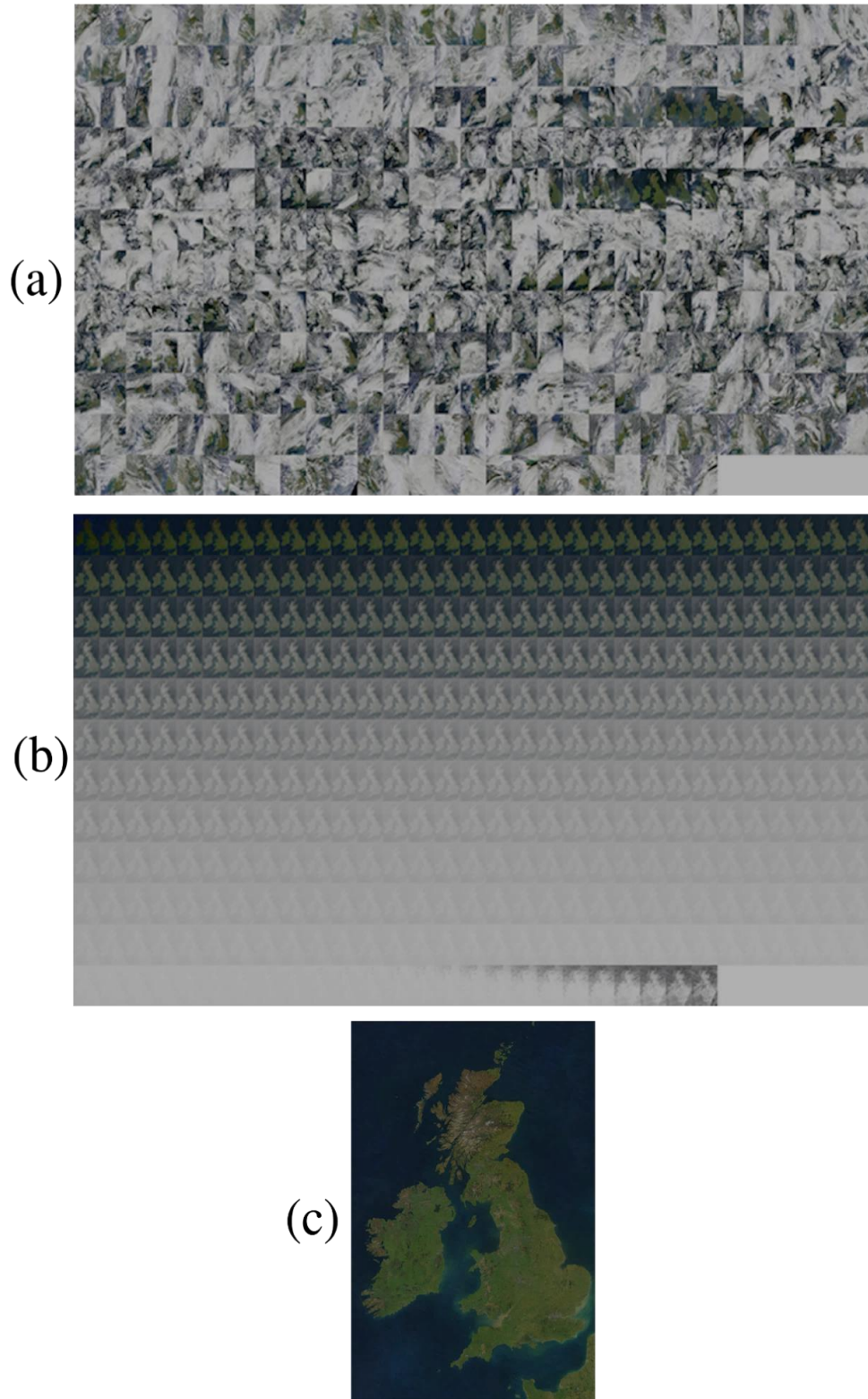


Figure 2.2 : Cloudless image generation procedure of Mapbox Co. a) Images of all year b) Normalized c) Cloudless image (Url-1).

2.1 Scientific Approach to Cloudless Mosaic Production

Averaging multitemporal satellite images is the most common method to create cloudless image for web basemaps. This method gives visually sufficient and good looking results although it may cause a loss of spectral information (Loyd, 2012). Methods which preserve spectral information is summarized in Introduction chapter. In this study, both visual appearance and spectral consistency are taken into account to develop a superpixel based binary classification approach to create cloudless images.

2.2 Cloud Types

Clouds are given Latin names corresponding to their appearance and height (Muller, 2016). See the following list;

Clouds are classified according to:

- Height, defined by altitude of cloud base.
 - o High: cirrus (Ci), cirrostratus (Cs), cirrocumulus (Cc)
 - o Middle: Altostratus (As), Altocumulus (Ac)
 - o Low: Stratus (St), stratocumulus (Sc), nimbostratus (Ns)
 - o Clouds with vertical development: cumulus (Cu), cumulus congestus (Towering Cumulus-TCU), cumulonimbus (Cb)

Meteorologists also categorize clouds according to precipitation. All of these different identification features make differences how we see cloud in images (Table 2.1, Figure 2.3).

Table 2.1 : Common cloud types and specifications (CIMSS, 2016).

| Cloud Level | Layer Clouds | Heap Clouds | Hybrid |
|---------------|--------------------------|--------------|--------------------------------|
| High | Cirrus \ Cirrostratus | Cirrocumulus | |
| Mid | Altostratus | Altocumulus | |
| Low | Stratus | Cumulus | Stratocumulus |
| Precipitating | Nimbostratus | | Cumulusnimbus (Thunderstorms!) |

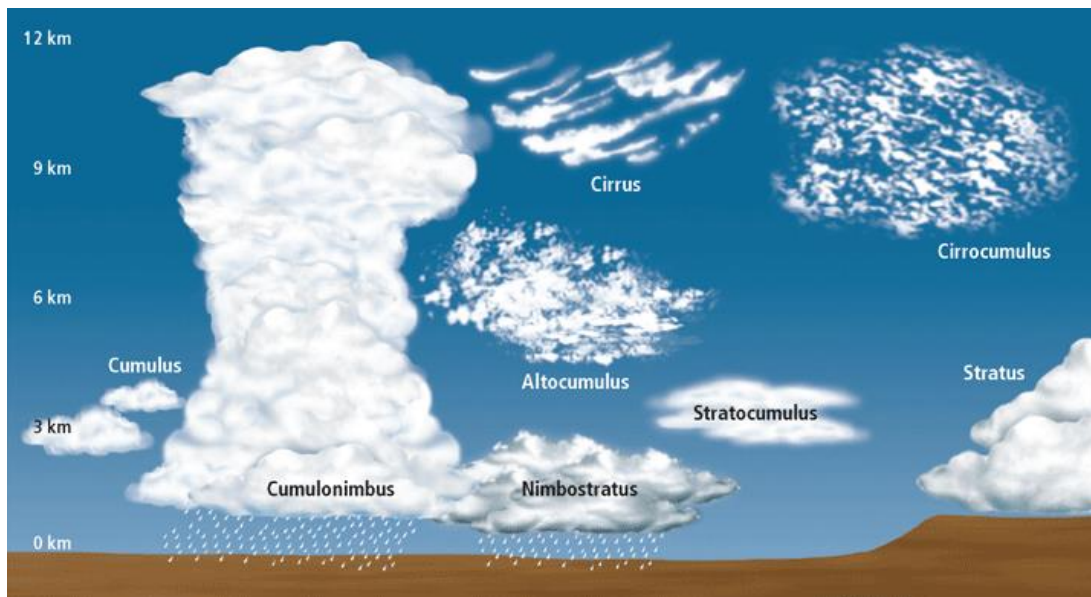


Figure 2.3 : Common cloud types with reference altitude chart (<https://laulima.hawaii.edu / Geography 101 Course Notes>).

Identification of clouds from satellite images is the main purpose of cloud classification process. Basic features for cloud identification can be listed such as; brightness, texture (shadow in VIS), pattern, edge definition, size and individual shape (Muller, 2016). Reflective characteristics of clouds are important to analyze how they seen in satellite images. All surfaces reflect varying amounts of sunlight (Table 2.2). Different types of clouds are also reflects different amount of sunlight according to their thickness.

Table 2.2 : Reflectance characteristics of different surfaces (From Radar and Satellite Weather Interpretation for Pilots, Lankford.).

| Surface Type | Albedo |
|---------------------|--------|
| Large Thunderstorm | 92% |
| Thick stratocumulus | 68% |
| Snow | 88-59% |
| Thin stratus | 42% |
| Thin cirrostratus | 32% |
| Forest | 12% |
| Water | 9% |

Normally clouds appear in satellite images bright white. Thin clouds allow most of sun's energy to pass through, reflecting very little sunlight which cause to appear gray in images and also mixture of surface materials' reflective characteristics. Also, gaps between small clouds allow some of the Earth's reflected energy through, when averaged with the clouds, the clouds appear grayer than normal. (Figure 2.4)

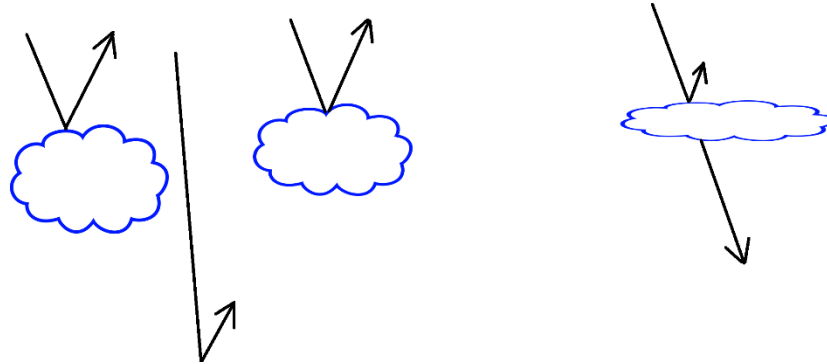


Figure 2.4 : Thin and thick clouds and reflective characteristics.



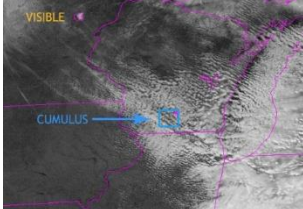




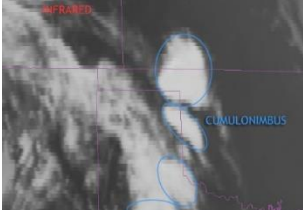





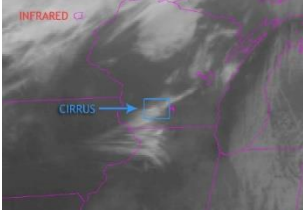
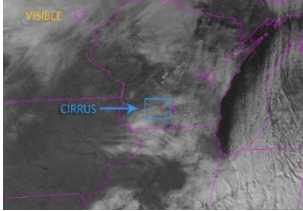

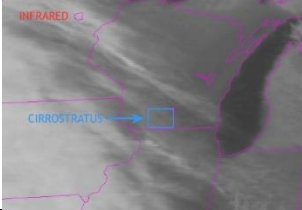

When you take into account all of these information about clouds, using both visible and infrared images to determine cloud and cloud types is the best method. Reference chart for cloud and cloud type discrimination from visible and infrared images are given in Table 2.3.

Table 2.3 : Cloud characteristics in visible and infrared images (Muller, 2016).

| IR Image | Visible Image | Possible Cloud Type |
|-----------------------|------------------------------|----------------------------|
| If clouds are: | AND if clouds appear: | |
| Cold | Thick (white) | Cb or Nimbostratus |
| Cold | Thin (gray) | Cirrus |
| Warm | Thick (white) | Low Stratus, Fog |
| Warm | Thin (gray) | Cumulus, stratocumulus |

Table 2.4 summarizes all common cloud types and their sample appearance from ground, visible and infrared satellite images (CIMSS, 2016).

Table 2.4 : Common cloud types from ground photo, infrared and visible satellite images.

| Photo From Ground | Infrared Satellite Images | Visible Satellite Images |
|--|---|--|
| Cumulus (Heap Clouds)  |  |  |
| Stratus (Layer Clouds)  |  |  |
| Cumulonimbus  |  |  |
| Altostratus  |  |  |
| Cirrus  |  |  |
| Cirrostratus  |  |  |

3. DATA AND PRE-PROCESSING

Cloning cloud areas is the main part of the thesis. As an initial step, all cloud pixels need to be classified accurately to start cloning process. Free distributed multitemporal dataset of Landsat-8 images are chosen for detection and cloning of cloud features. Using thermal bands of Landsat-8 images are also important for discrimination of cloud and snow features.

Four different Landsat-8 path-rows are selected as study area which have different land use characteristics and cloud covers between 10% and 30%. Evaluating results of the algorithm in different regions which have different surface characteristics is important to test transferability. Figure 3.1 shows the geographical distribution of selected images.

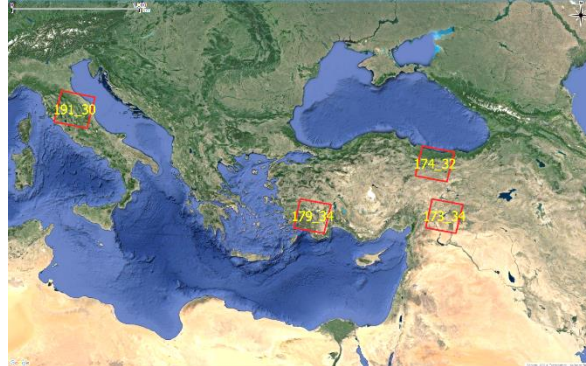


Figure 3.1 : Study area and distribution of selected images.

3.1 Landsat-8

Landsat-8 is an American Earth observation satellite launched on February 11, 2013. It is the eighth satellite of the Landsat program; the seventh to reach orbit successfully. Originally called the Landsat Data Continuity Mission (LDCM), it is a collaboration between NASA (National Aeronautics and Space Administration) and the United States Geological Survey (USGS) (Table 3.1). Landsat-8 scenes are processed by Amazon team and available after hours of acquisition. Landsat-8 is freely distributed

over web and Amazon Cloud Service (AWS). Information about OLI (Operational Land Imager) and thermal bands is given in Table 3.2.

Table 3.1 : Technical details about Landsat-8 (USGS, 2015).

| Landsat-8 in detail |
|---|
| Product type: Level 1T (terrain corrected) |
| Output format: GeoTIFF |
| Pixel size: 15 meters/30 meters/100 meters (panchromatic/multispectral/thermal) |
| Map projection: UTM (Polar Stereographic for Antarctica) |
| Datum: WGS 84 |
| Orientation: North-up (map) |
| Resampling: Cubic convolution |
| OLI Accuracy: 12 meters circular error, 90-percent confidence |
| TIRS Accuracy: 41 meters circular error, 90-percent confidence |

Table 3.2 : Landsat 8-OLI and Thermal Infrared Sensor (TIRS) spectral band characteristics (USGS, 2015).

| Bands | Wavelength (micrometers) | Resolution (meters) |
|-------------------------------------|--------------------------|---------------------|
| Band 1 - Coastal aerosol | 0.43 - 0.45 | 30 |
| Band 2 - Blue | 0.45 - 0.51 | 30 |
| Band 3 - Green | 0.53 - 0.59 | 30 |
| Band 4 - Red | 0.64 - 0.67 | 30 |
| Band 5 - Near Infrared (NIR) | 0.85 - 0.88 | 30 |
| Band 6 - SWIR 1 | 1.57 - 1.65 | 30 |
| Band 7 - SWIR 2 | 2.11 - 2.29 | 30 |
| Band 8 - Panchromatic | 0.50 - 0.68 | 15 |
| Band 9 - Cirrus | 1.36 - 1.38 | 30 |
| Band 10 - Thermal Infrared (TIRS) 1 | 10.60 - 11.19 | 100 * (30) |
| Band 11 - Thermal Infrared (TIRS) 2 | 11.50 - 12.51 | 100 * (30) |

3.1.1 Automatic Download Tool

Landsat programs is a state-of-art earth observation program of USGS (United States Geological Survey) over decades. After 2015, Amazon Cloud Services Company announced that each Landsat images will be available in cloud disk space for easy downloading and usage purposes after a short period of time after acquisition (Amazon, 2015). In last quarter of 2016, Google also announced that more than 4 millions of Landsat data is available on Google Cloud Platform (Birch, 2016). In this study, a graphical user interface for selection of appropriate study site is developed.

Users can select appropriate Path/Row and Date for study area by drawing a rectangle on map. Users also can select which image to work with from all multitemporal data set (Figure 3.2 and Figure 3.3).

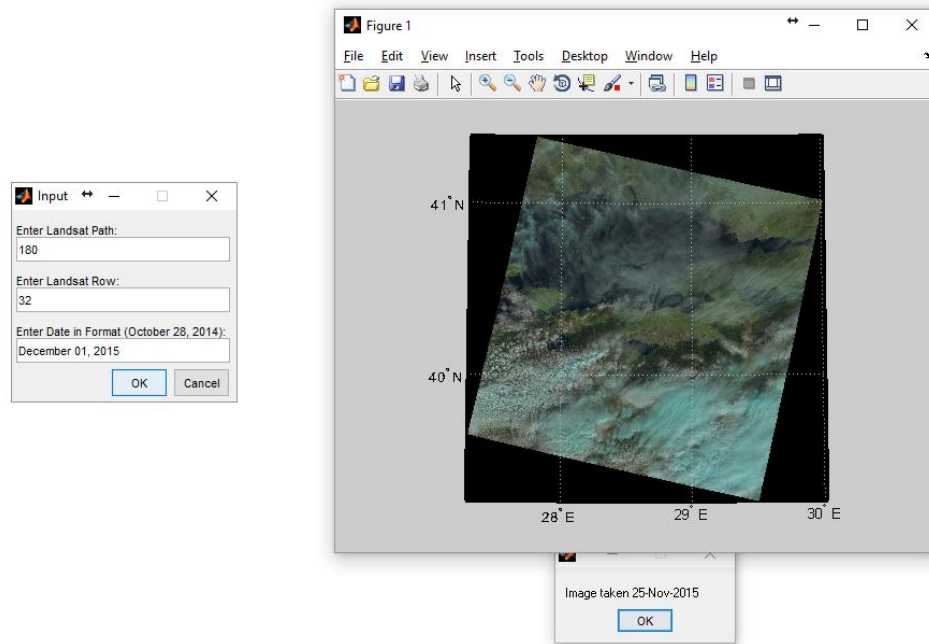


Figure 3.2 : Landsat Path/Row/Date selection and quicklook.

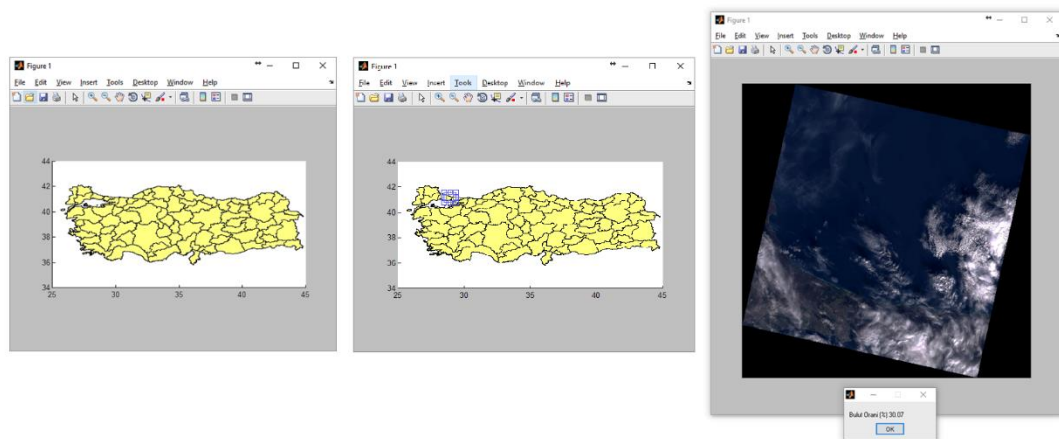


Figure 3.3 : Landsat study area selection GUI and downloaded image.

3.2 Calibration of Data

Landsat 8 data is provided as raw DN (Digital Number) numbers. Data can be rescaled to the Top of Atmosphere (ToA) reflectance and radiance using radiometric rescaling coefficients stored in the product metadata file (MTL file) (Figure 3.4). By this conversion, image data is converted to physically meaningful units. Metadata file also

contains the thermal constants needed to convert TIRS data to the at-satellite brightness temperature.

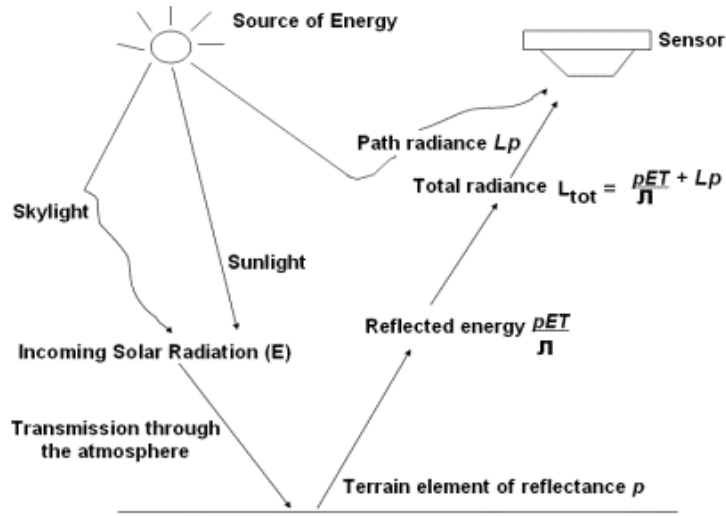


Figure 3.4 : Source of energy, radiance and reflectance (Source: Lillesand and Kiefer, 2002).

3.2.1 Radiance

Radiance is described as, radiation reflected by a surface and falls within a given solid angle in specific direction. OLI and TIRS bands can be converted to ToA spectral radiance using the scaling factors of data which is given in metadata file for each scene (equation 3.1):

$$L_{\lambda} = M_L Q_{cal} + A_L \quad (3.1)$$

L_{λ} = ToA spectral radiance (Watts / (m² x srad x μm))

M_L = Band-specific multiplicative rescaling factor

A_L = Band-specific additive rescaling factor

Q_{cal} = Pixel values (DN)

3.2.2 Reflectance

Reflectance is described as, fraction of incident electromagnetic power that is reflected at an interface. Using radiometric corrected data for remote sensing analysis is important for multitemporal image analysis. OLI data can be converted to ToA planetary reflectance after radiance conversion using reflectance rescaling coefficients given in the product metadata file (MTL file). Equation 3.2 is used to convert DN values to ToA reflectance for OLI data (USGS, 2015).

$$\rho_{\lambda} = M_p Q_{cal} + A_p \quad (3.2)$$

$\rho_{\lambda'}$ = ToA reflectance, without correction for solar angle.

M_p = Band-specific rescaling factor

A_p = Band-specific additive rescaling factor

Q_{cal} = Pixel values (DN)

Also, sun angle correction is applied to ToA reflectance values by using equation (3.3)

$$\rho_{\lambda} = \frac{\rho_{\lambda'}}{\cos(\theta_{SE})} = \frac{\rho_{\lambda'}}{\sin(\theta_{SZ})} \quad (3.3)$$

ρ_{λ} = ToA reflectance

θ_{SE} = Sun elevation angle

θ_{SZ} = Solar zenith angle; $\theta_{SZ} = 90^{\circ} - \theta_{SE}$

After all of these conversions, all processes are applied to reflectance images (Figure 3.5).

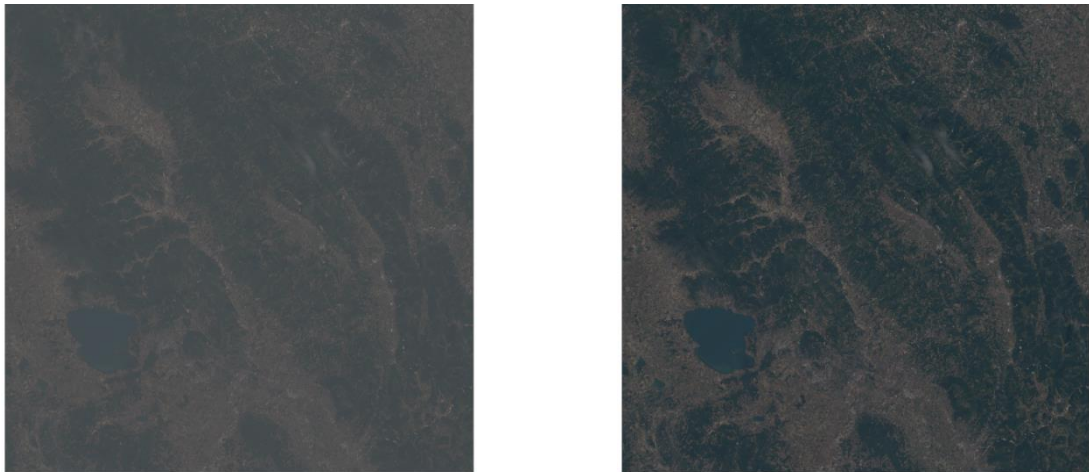


Figure 3.5 : Landsat-8 image radiometric calibration (left) Raw Landsat-8 (right) ToA reflectance calibrated.

3.2.3 Brightness Temperature

The apparent temperature of the surface assuming a surface emissivity of 1 (one). Setting the emissivity to one is equivalent to assuming the target is a blackbody, so the brightness temperature is defined as the temperature a blackbody would be in order to produce the radiance perceived by the sensor. Brightness temperature is a descriptive measure of radiation in terms of the temperature of a hypothetical blackbody emitting an identical amount of radiation at the same wavelength. The brightness temperature is obtained by applying the inverse of the Planck function to the measured radiation. Depending on the nature of the source of radiation and any subsequent absorption, the

brightness temperature may be independent of, or highly dependent on, the wavelength of the radiation (GES DISC, 2016).

TIRS data can be converted from radiance to BT by using the thermal rescaling given in metadata file by using equation 3.4 (USGS, 2015).

$$T = \frac{K_2}{\ln\left(\frac{K_1}{L_\lambda} + 1\right)} \quad (3.4)$$

T = At-sensor brightness temperature (K)

L_λ = ToA spectral radiance (watts/ (m² x srad x μm))

K_1, K_2 = Band-specific thermal conversion constant

Brightness temperature information is used in cloud detection algorithm which shows lower temperature values in cloud regions compared to other regions. TIR2 channel which is indicating better cloud discrimination is used for cloud and shadow detection (Figure 3.6).

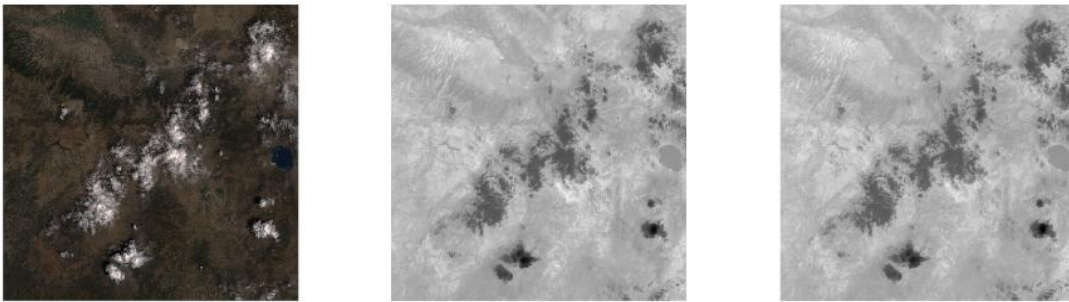


Figure 3.6 : Landsat-8 image converted brightness temperature.

3.2.4 Atmospheric Correction

Atmospheric correction is simply described as a process of removing the atmospheric effects in satellite images. The effects of atmosphere should be considered to measure and calculate surface reflectance. Land surface reflectance is described as (Moran et al., 1992) (equation 3.5);

$$\rho = \frac{[\pi \times (L_\lambda - L_p) \times d^2]}{[T_v \times ((ESUN_\lambda \times \cos\theta_s \times T_z) + E_{down})]} \quad (3.5)$$

where:

L_p : path radiance

T_v : atmospheric transmittance in the viewing direction

T_z : atmospheric transmittance in the illumination direction

E_{down} : downwelling diffuse irradiance

Atmospheric measurements are needed for applying this formula in order to calculate surface reflectance. Alternatively, image-based techniques are developed for the calculation of these parameters when there is no change for field measurements (Chavez, 1996).

The Dark Object Subtraction (DOS) is one of the state-of-art image-based atmospheric correction method. Assumption of this method is that some pixels in image are in complete shadow and radiance of them at satellite are caused by path radiance of atmospheric scatter. Another support of this assumption is the fact of very few land cover types on the earth surface are absolute black. Compared with other advanced atmospheric correction methods, accuracy of image-based techniques are lower than physically-based methods. Furthermore, they are very effective for estimation of land surface reflectance when no atmospheric measurements are available as they can (Congedo, 2016).

The path radiance by definition of (Sobrino et al, 2004) (equation 3.6):

$$L_p = L_{\min} - L_{DO1\%} \quad (3.6)$$

where:

L_{\min} = “radiance that corresponds to a digital count value for which the sum of all the pixels with digital counts lower or equal to this value is equal to the 0.01% of all the pixels from the image considered” (Sobrino et al, 2004, p. 437)

$L_{DO1\%}$ = radiance of Dark Object, assumed to have a reflectance value of 0.01

L_{\min} for Landsat images (equation 3.7):

$$L_{\min} = M_L * DN_{\min} + A_L \quad (3.7)$$

The radiance of dark object by definition of (Sobrino et al, 2004) (equation 3.8):

$$L_{DO1\%} = 0.01 * [(ESUN_{\lambda} * \cos\theta_s * T_z) + E_{\text{down}}] * T_v / (\pi * d^2) \quad (3.8)$$

Then path radiance is (equation 3.9):

$$L_p = M_L * DN_{\min} + A_L - 0.01 * [(ESUN_{\lambda} * \cos\theta_s * T_z) + E_{\text{down}}] * T_v / (\pi * d^2) \quad (3.9)$$

There are several DOS techniques developed based on different assumptions of T_v , T_z , and E_{down} (e.g. DOS1, DOS2, DOS3, DOS4). Basic technique is the DOS1, which uses following assumptions (Moran et al, 1992);

- $T_v = 1$, $T_z = 1$, $E_{\text{down}} = 0$

Then path radiance is (equation 3.10):

$$L_p = M_L * DN_{min} + A_L - 0.01 * ESUN_{\lambda} * \cos\theta_s / (\pi * d^2) \quad (3.10)$$

Final land surface reflectance is (Figure 3.7) (equation 3.11):

$$\rho = [\pi * (L_{\lambda} - L_p) * d^2] / (ESUN_{\lambda} * \cos\theta_s) \quad (3.11)$$

For Landsat 8, ESUN calculation formula is given in equation 3.12.

$$ESUN = (\pi * d^2) * RADIANCE_MAXIMUM / REFLECTANCE_MAXIMUM \quad (3.12)$$

where RADIANCE_MAXIMUM and REFLECTANCE_MAXIMUM can be found in metadata file.

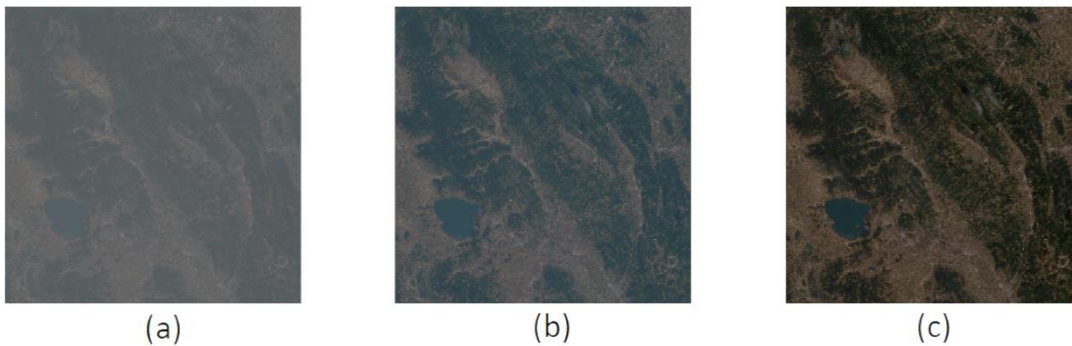


Figure 3.7 : Landsat-8 image calibration steps (a) RAW Landsat 8 (b) ToA reflectance calibrated (c) DOS 1 Atmospheric corrected.

4. CLOUD AND SHADOW DETECTION

The primary limitation of passive remote sensing sensors is their sensitivity to weather conditions during data acquisition. Land scenes are, on average, approximately 35% cloud covered globally (Ju et al, 2008), significantly reducing the availability of cloud-free satellite images. Detection of cloud and shadow areas from satellite images is an important step for many analyses. In this chapter, cloud and shadow detection methodology is described in detail.

Proposed cloud detection algorithm is based on usage of OLI (Operational Land Imager) and thermal bands. OLI bands are calibrated to ToA: Top of Atmosphere Reflectance and thermal bands are converted to brightness temperature to use in this algorithm. Cloud areas are identified using ruleset-based classification applied on reflectance calibrated images by following superpixel segmentation of satellite image. Following classification of cloud areas, cloud shadows are classified by evaluating spectral test and neighbourhood relations with cloud regions. Developed method is a simplified version of ACCA and Fmask algorithms. Cloud and shadow masks obtained by Fmask and results obtained by our method are compared, and results are evaluated. General workflow chart of all steps concluded in cloud and shadow detection process is given in Figure 4.1.

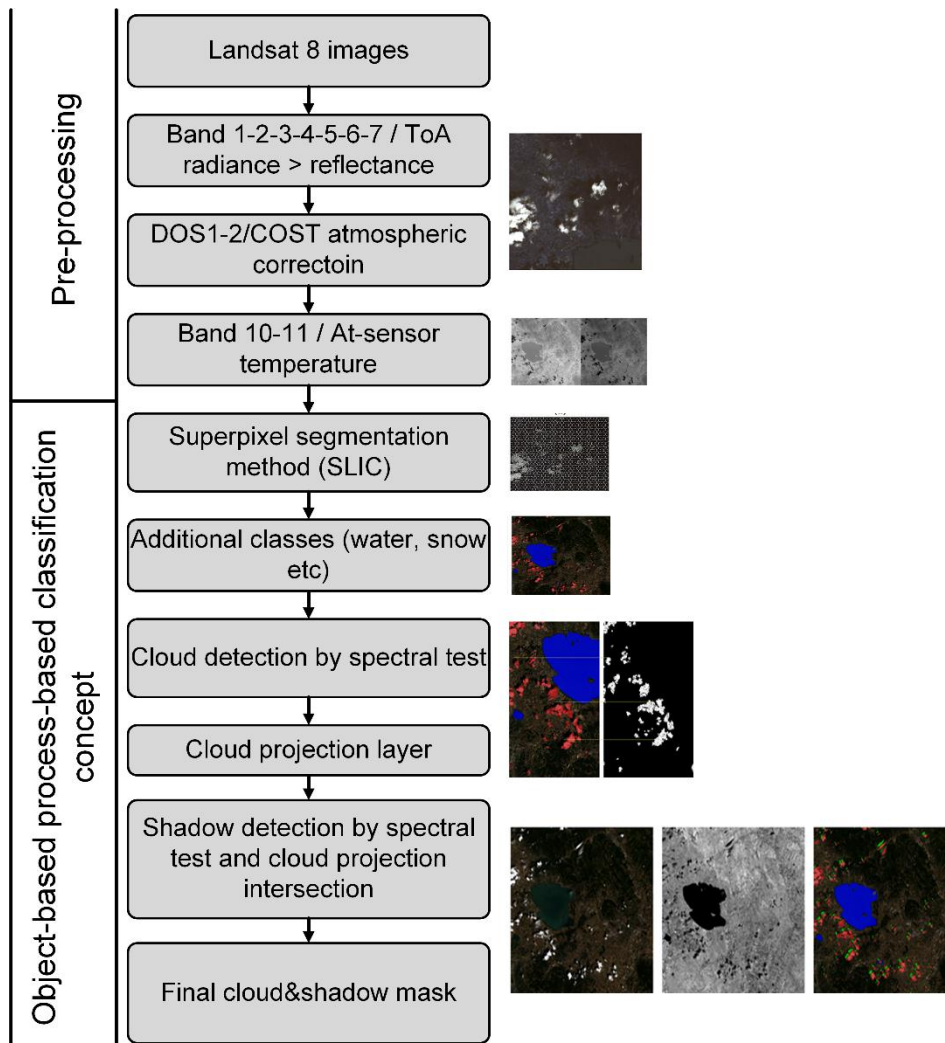


Figure 4.1 : General workflow chart of study.

4.1 Segmentation

Generally, clouds and shadows are combination of pixel groups in satellite images despite spreaded as small pixels. Pixel by pixel processing of satellite image for binary classification works needs much more processing load than using superpixels. Based on a concept of merging homogenous pixels to pixel groups, Object Based Image Analysis (OBIA) concept is merging millions of pixels into thousands of superpixels to process easily. Clouds and shadows are good example to use superpixels methods which both of them occur as patches in images. Not only spectral information but also parameters like texture, pattern, area, linearity etc. can be used for classification. In this chapter, OBIA analysis of thesis is described in detail. Beyond using word of segment for pixel groups, “superpixel” term of computer vision is used for describing homogenous pixel groups.

4.1.1 SLIC Segmentation

Superpixels are used to combine pixels into meaningful groups to create pixel groups. Merging pixels which have similar information is speeding up image processing tasks. SLIC (Simple Linear Iterative Clustering) algorithm is an efficient method for segmentation of image which is based on spatially localized version of K-means clustering method. Fundamental specifications and advantages of SLIC method are evaluated in Achanta et al. (2002).

SLIC divides image into a $M \times N$ regular grids. M and N values are given as an input, where (equation 4.1)

$$M = \frac{imageWidth}{regionSize}, N = \frac{imageHeight}{regionSize} \quad (4.1)$$

A superpixel is processed by initializing from each grid center (equation 4.2)

$$x_i = round_i \frac{imageWidth}{regionSize}, y_i = round_j \frac{imageWidth}{regionSize} \quad (4.2)$$

Following this step, regions are obtained by running K-means clustering, started from the centers (equation 4.3).

$$C = \left\{ \begin{array}{l} \Psi(x_i, y_j) \\ i = 0, 1, \dots, M - 1 \\ j = 0, 1, \dots, N - 1 \end{array} \right\} \quad (4.3)$$

K-means uses the standard Lloyd algorithm alternating by assigning pixels to the closest centers (Lloyd, 1982). Differences of SLIC compared to standard K-means is that each pixel can be assigned only to the center which comes from the neighbour tiles. After creation of superpixels, each superpixel is taken into account to check if area is less than minimum region size value which is taken as an input from user (Vedaldi and Fulkerson, 2010). Results of SLIC algorithm which is applied to cloud image are shown in Figure 4.2.

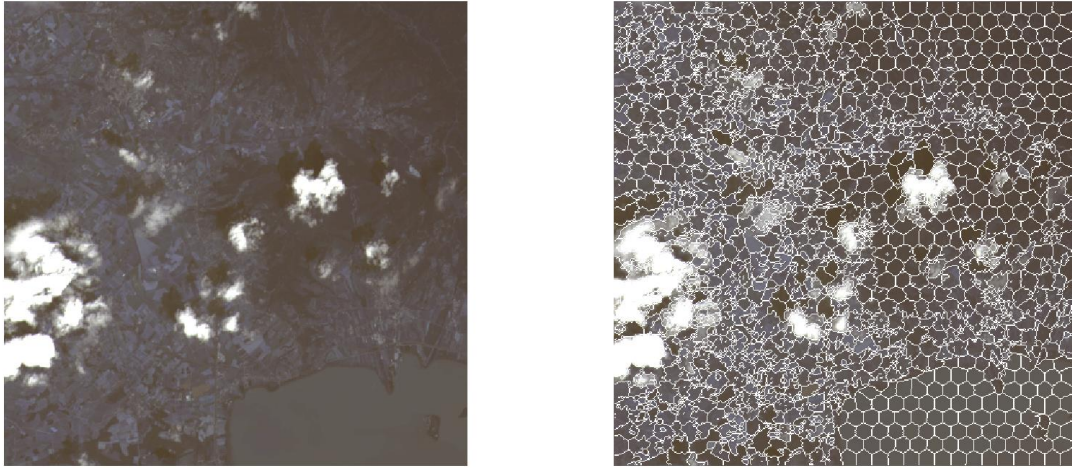


Figure 4.2 : Results of SLIC algorithm applied to cloud image (left) Original image (right) SLIC superpixel segmentation result.

4.2 Cloud Detection

After superpixel segmentation of satellite images, cloud detection steps are described in detail in this chapter.

4.2.1 Classification of Additional Classes (Water and Snow)

Not only clouds, but also higher buildings, hills and factors which cause height difference can also cause shadows according to sun azimuth. Shadows and water bodies are misclassified to each other because of their dark behaviour. In this study, NDWI (Normalized Difference Water Index) and cloud projection methods are used to overcome these two misclassification problems mentioned above (Gao, 1996).

NDWI values are calculated to prevent misclassification of water bodies and shadow areas to each other. The constant threshold is used to classify water bodies automatically (equation 4.4) (Figure 4.3).

$$NDWI = \frac{NIR - Green}{NIR + Green} \quad (4.4)$$

$$(Water - NDWI < -0.2)$$

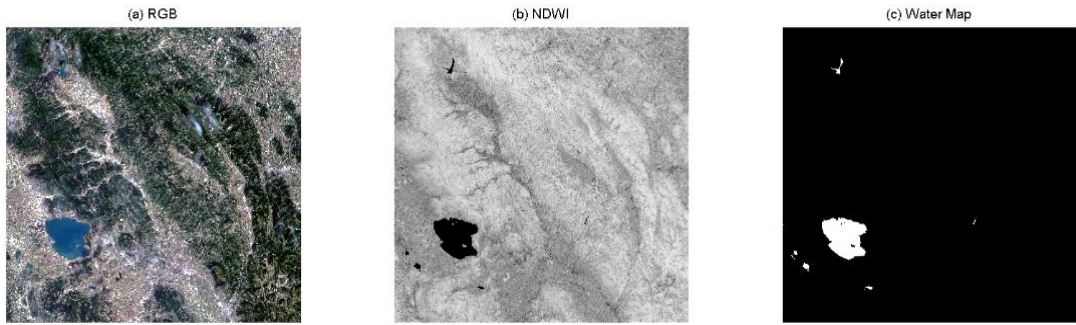


Figure 4.3 : (a) Original RGB image (b) NDWI Index (c) Water classification based on NDWI threshold (scene ID: LC81910302014163LGN00).

NDSI is a normalized difference of two bands (Green and SWIR1) to map snow. Beside the advantage of using the thermal infrared band, NDSI information is also added to the procedure to cope with difficulties caused by snow-covered areas which have bright and cold temperature features (equation 4.5). NDSI index is used for discrimination of clouds and snow cover (Hall and Riggs, 2011). Pixels which have NDSI values greater than 0.8 are classified as snow (USGS, 2015) (Figure 4.4).

$$NDSI = \frac{Green - SWIR\ 1}{Green + SWIR\ 2} \quad (4.5)$$

(Snow NDSI > 0.8)

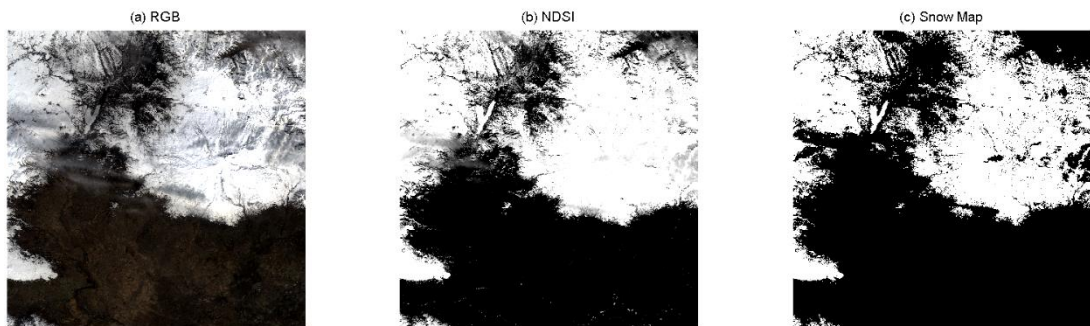


Figure 4.4 : (a) Original RGB image (b) NDSI index (c) Snow classification based on NDSI threshold (scene ID: LC81700322015067LGN00).

4.2.2 Cloud Classification Background (Thermal Band Usage)

Thermal band usage is also easing the process of opaque cloud classification. Band ratio of cloud pixels compared to other land cover types are resulting in higher values in cloud regions which ease thresholding process for cloud detection. Cloud classification method is developed within a multi-criteria structure shown in Figure 4.1. Pixels have temperature value less than 300K are classified as cloud candidate by using information provided by USGS (Figure 4.5-Figure 4.6).

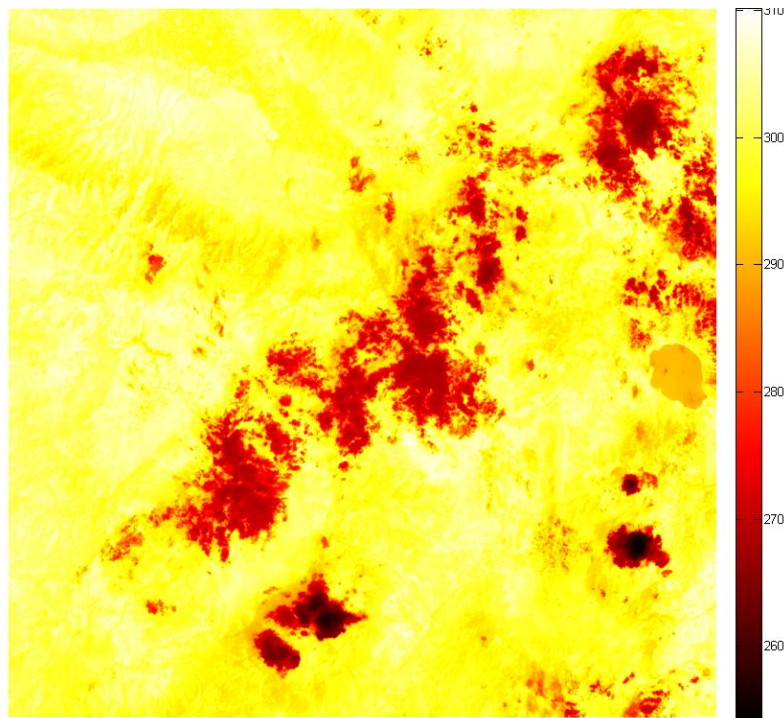


Figure 4.5 : Colormap of thermal infrared 2 band (LC81790342014207LGN00).

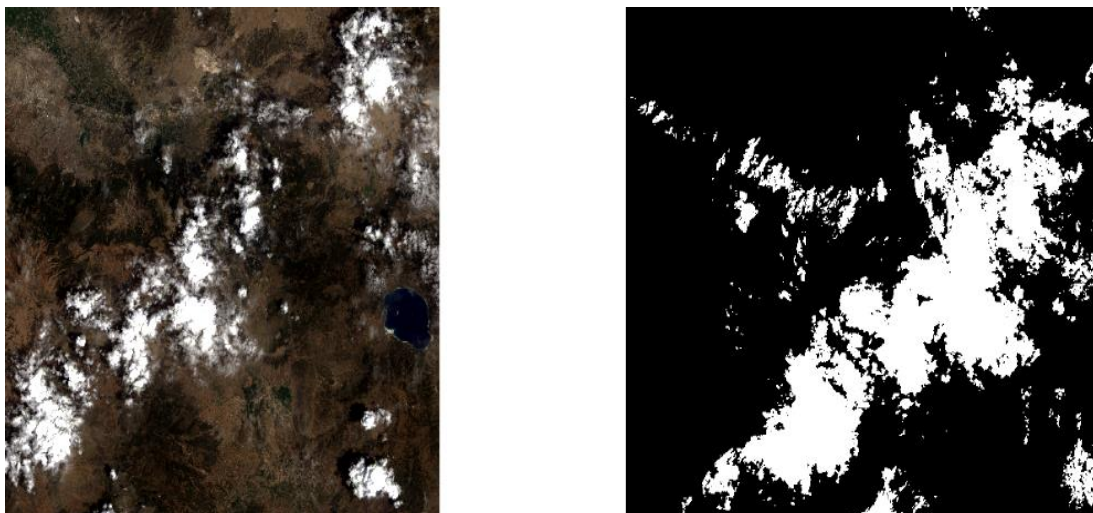


Figure 4.6 : (a) Original RGB image (b) Pixels which are smaller than 300K in TIR2 band (Cloud candidate).

4.2.3 Multi-Criteria Cloud Classification Approach

Detection of cloud features from Landsat image is started by identification of spectral characteristics of clouds. Spectral signatures collected from image are shown on Figure 4.7. Algorithm is developed on the basis of these signatures.

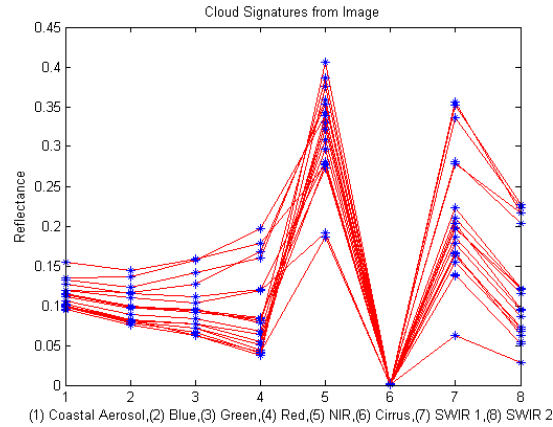


Figure 4.7 : Cloud spectral signatures collected from image.

As seen in Figure 4.7, cloud areas have high brightness values in NIR (Band 5), and SWIR (Band 7) which makes them easily distinguishable in those regions. In addition to this, information about characteristics of bright objects on the blue band is taken into account and values of these three bands are multiplied with each other. Cloud shadows are discriminated from other features by dividing thermal channel to the multiplication of two bands based on information of low-temperature characteristic of cloud features on thermal infrared bands (Table 4.1) (equation 4.6) (Figure 4.8).

$$Index_{cloud} = \frac{NIR * SWIR1 * Blue}{Thermal 2} \quad (4.6)$$

Table 4.1 : Cloud classification criteria.

| Feature | Threshold |
|----------------------------|---|
| NDSI | Not snow (NDSI < 0.6) |
| Thermal Infrared | <300 Kelvin |
| Cloud Classification Index | The dynamic threshold which comes from brightest object cluster of the image. |

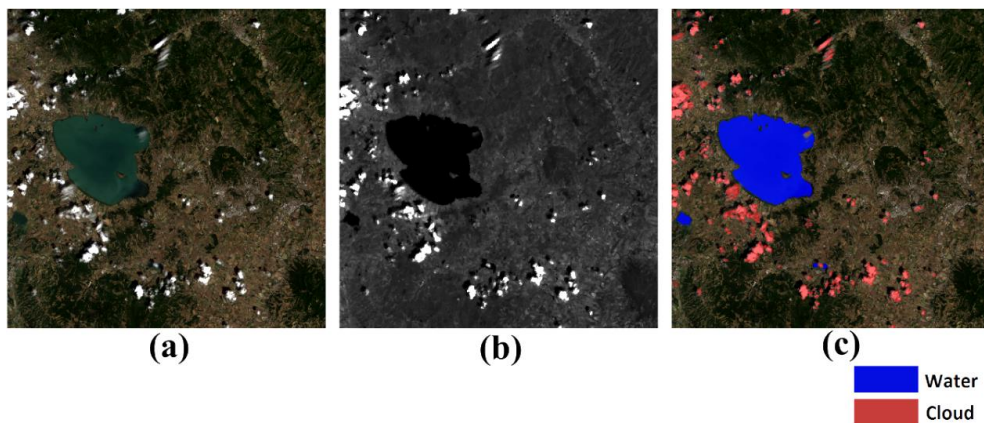


Figure 4.8 : (a) Original image (b) Cloud detection index (c) Classified cloud areas.

4.3 Shadow Classification

Similar to cloud features, cloud shadow classification method is also developed based on interpretation of spectral signatures which are collected from cloud shadow areas (equation 4.7). Cloud shadow areas are distinguished easily by using this index which eases dynamic thresholding for shadow detection.

$$Index_{shadow} = \frac{NIR * SWIR 1}{Red} \quad (4.7)$$

Neighbour edges of cloud and shadow classifications are added to these classified areas by region growing to complete all classification process.

4.4 Cloud and Cloud Shadow Relation (Cloud Projection Method)

Beyond shadow classification index, projections of cloud features to a specific distance are calculated according to sun azimuth angle which comes from image metadata (Figure 4.9; Figure 4.10). It is used to prevent misclassification of cloud shadow features with other shadows. This candidate cloud projection layer is a qualifier to ensure objects classified as cloud shadows are associated with cloud pixels. Methods developed within this thesis follows, Luo et al. (2008); Hughes and Hayes (2014); Braaten et al, (2015); Huang et al, (2010) and Zhu and Woodcock, (2012) by focusing on superpixel segmented image pixels.

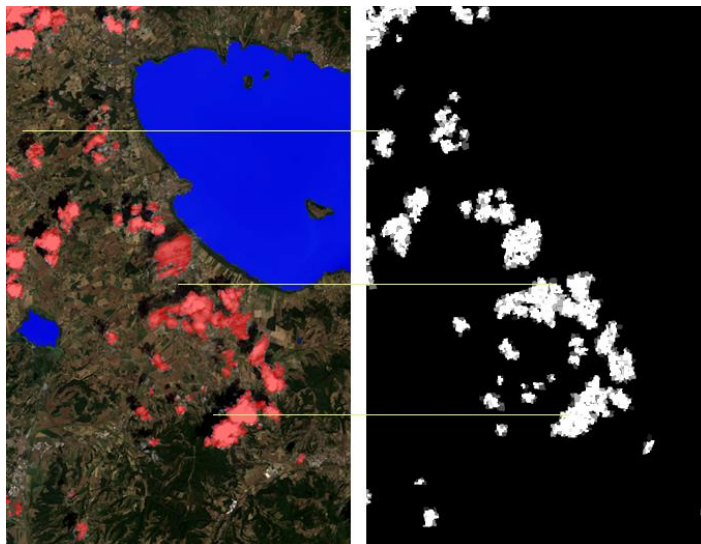


Figure 4.9 : Relationship between clouds and cloud shadow projections (cloud projection layer (left), cloud layer (right)).

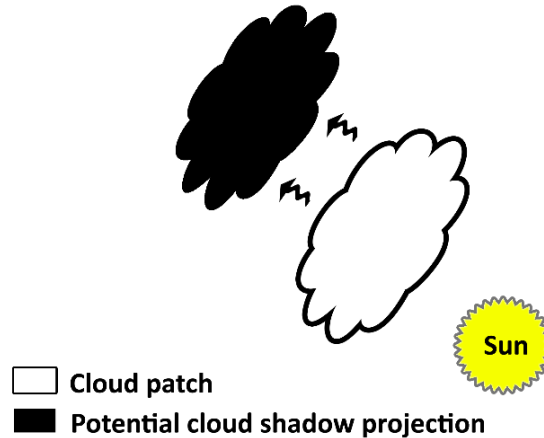


Figure 4.10 : Cloud and cloud shadow projection relation.

Sun azimuth angle is an angle which is measured clockwise from the north while image acquisition (Figure 4.11). Clouds and their shadows are related by their relative locations depending on the image acquisition time and the sun location (Le Hégarat-Masclé and André, 2009).

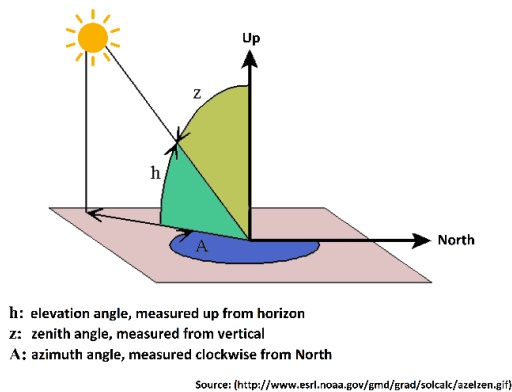


Figure 4.11 : Sun elevation, sun azimuth and zenith angle.

Cloud-shadow distance is designated as 30 pixels based on tests applied on the image. These projected areas are potential cloud shadow patches. Intersections of these areas with cloud shadow index are used to identify final cloud shadow classification (Table 4.2, Figure 4.12).

Distance between clouds and cloud shadow superpixels is also important indicator to correlate clouds with their shadows. 100 pixels buffer is used to check shadows if they have clouds around them. Size of cloud shadows is also another indicator to understand if they are related to clouds. Shadows of clouds are always smaller than their connected clouds (Ho and Cai, 1996). Shadows bigger than clouds are eliminated from classification.

Table 4.2 : Shadow classification rules.

| Feature | Threshold |
|----------------------------|---|
| NDWI | Not water |
| Potential cloud projection | Intersection |
| Shadow detection index | The dynamic threshold which comes from darkest object cluster of the image. |
| Closeness | Clouds in 100 pixels buffer |
| Size | Size < Cloud size |
| Direction | Relation with sun location |

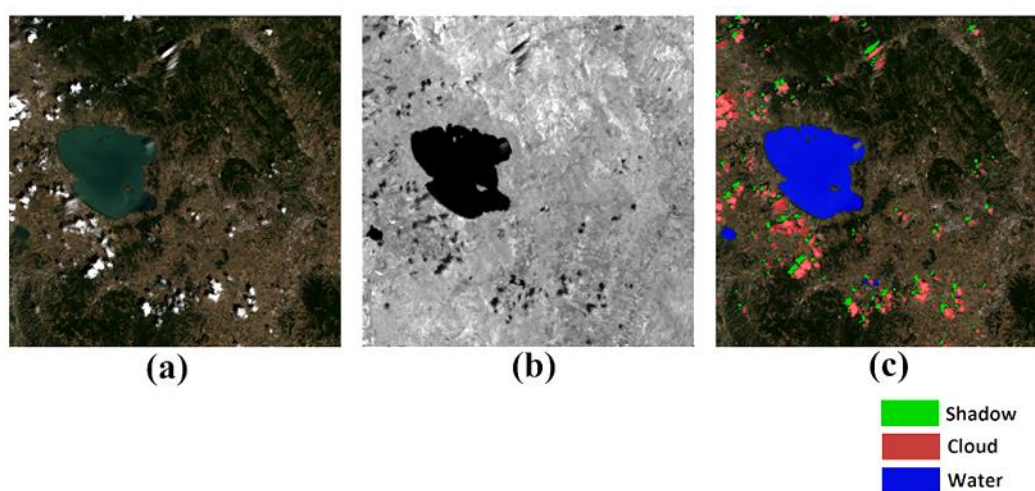


Figure 4.12 : (a) Original image (b) Shadow detection index (c) Classified cloud shadow areas.

4.5 Results of Cloud and Shadow Detection

Results from our approach and Fmask are compared in Figure 4.13 for four different study areas. As seen in Figure 4.14, our method gives more efficient results than Fmask regarding the geometrical accuracy of cloud and shadow structures because of its segmentation-based approach.

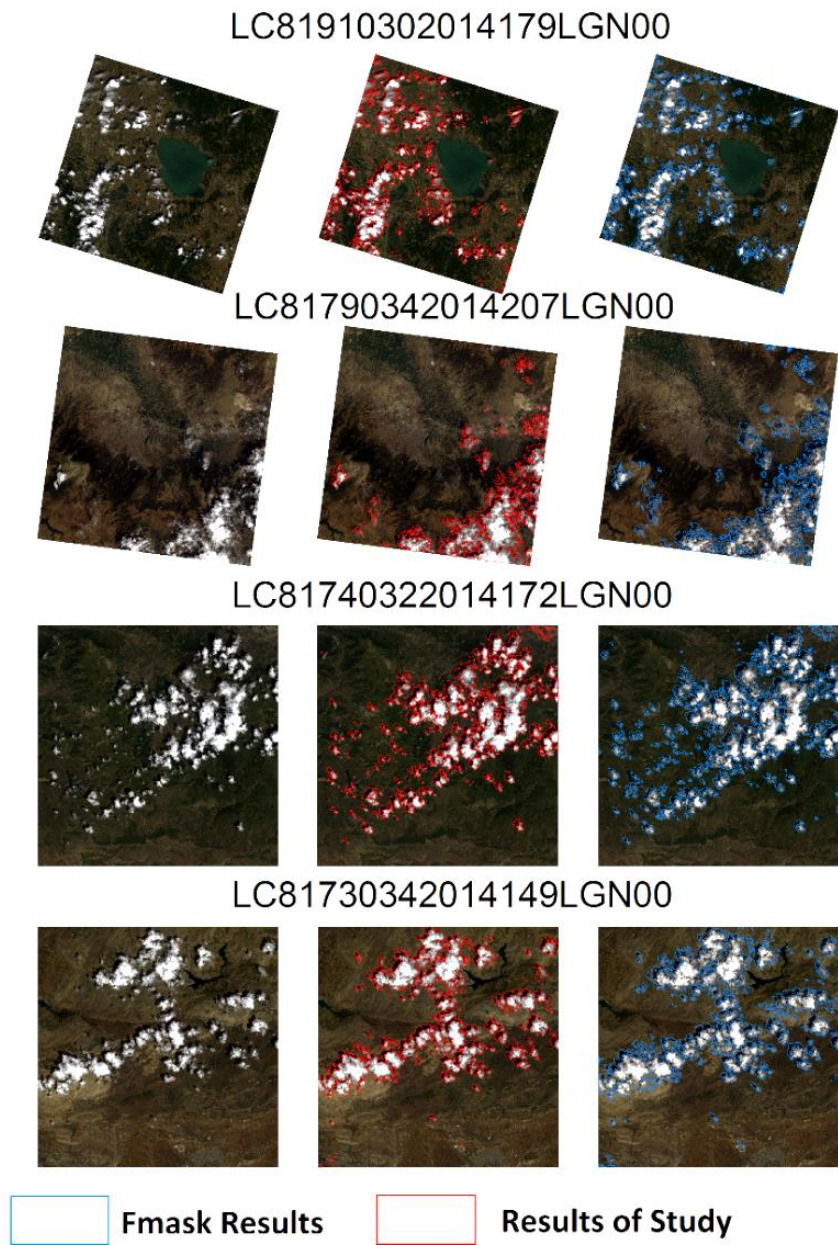


Figure 4.13 : Results of our approach compared to Fmask method.

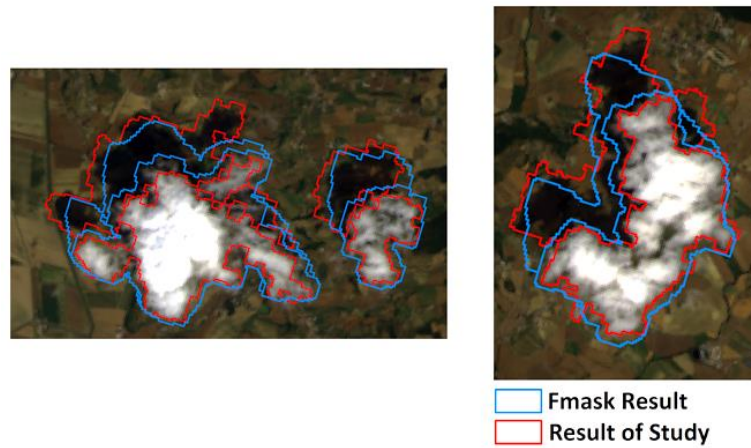


Figure 4.14 : Detailed area from results.

Zoom level is not sufficient to spot little details in Figure 4.13. Images taken from two different parts of the image are zoomed up in Figure 4.14 to show details and analyse them. Fmask and our method are both giving sufficient results for cloud and shadow detection.

4.6 Accuracy Assessment

For binary classification applications, using precision and recall metrics give better understanding to evaluate accuracy of classification. Precision is the number of True Positives divided by the number of True Positives and False Positives (Equation 4.8). In other words, it is the number of positive predictions divided by the total number of positive class values predicted. It is also called the Positive Predictive Value (PPV) (Table 4.3).

$$\text{Precision} = \text{positive predictive value} = \frac{TP}{TP+FP} = p \quad (4.8)$$

Table 4.3 : Accuracy indicators.

| | Result of detection: positive | Result of detection: negative |
|-----------------|-------------------------------|-------------------------------|
| Truth: positive | TP | FN |
| Truth: negative | FP | TN |

(TP: True positive, TN: True negative, FP: False positive, FN: false negative)

Recall is the number of True Positives divided by the number of True Positives and the number of False Negatives. In other words; it is the number of positive predictions divided by the number of positive class values in the test data. It is also called Sensitivity or the True Positive Rate (TPR). Recall can be thought of as a measure of a classifiers completeness. A low recall indicates many False Negatives (Figure 4.15) (Equation 4.9).

$$\text{Recall} = \text{true positive rate} = \text{sensitivity} = \frac{TP}{TP+FN} = r \quad (4.9)$$

$$\text{F measure} = \frac{2pr}{p+r}$$

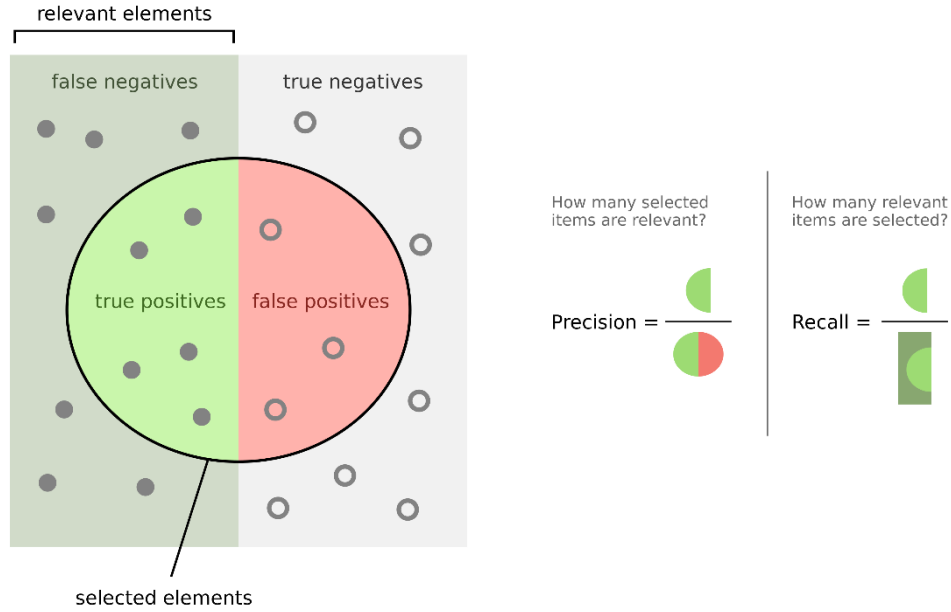


Figure 4.15 : Graphical descriptions of TP, FP, Precision and Recall (Source: Wikipedia).

Ground truths of both cloud and shadow patches are manually digitized to calculate accuracy metrics for evaluation of results. Accuracy metrics of cloud and shadow detection results can be seen in Table 4.4.

Table 4.4 : Accuracy metrics.

| | Cloud | | Shadow | |
|--------------------------|------------|-----------|------------|-----------|
| | Our method | FMASK | Our method | FMASK |
| (units: m ²) | | | | |
| FN | 49019439 | 10408916 | 18094272 | 34678429 |
| FP | 15113284 | 73504582 | 48253971 | 50534909 |
| TP | 207835135 | 246445658 | 86651967 | 54631517 |
| Precision | 0,93 | 0,77 | 0,64 | 0,52 |
| Recall | 0,81 | 0,96 | 0,83 | 0,61 |
| F measure | 0,87 | 0,85 | 0,72 | 0,56 |
| Total Classified | 222901200 | 319786200 | 144836100 | 95393700 |
| Total GT | 256854574 | 256854574 | 113219107 | 113219107 |
| TP / Total Classified | 0,93 | 0,77 | 0,60 | 0,38 |

Precision and recall rates of our study are better than Fmask for four different test sites we used. Fmask method detects cloud with a bigger confidence interval which causes more classified areas. In this case, accuracy of two methods are also compared to a basic True Positive / Total Classified metric to understand classification accuracy. Fmeasure is also another metric which is commonly used for evaluation of binary

classification results. Results show that two methods show similar accuracy for cloud detection while our method shows more accuracy in shadow classification which uses cloud projection method to improve cloud&shadow relationships.

5. CLOUD CLONING

Information reconstruction of images has become an active research topic in the fields of remote sensing, computer vision, and computer graphics because of its practical importance. Before information reconstructions of cloud covered images, accurate detection of cloud and shadow patches is the main step of cloud cloning process. Cloud and shadow patches are the main input of cloning algorithm (Figure 5.1).

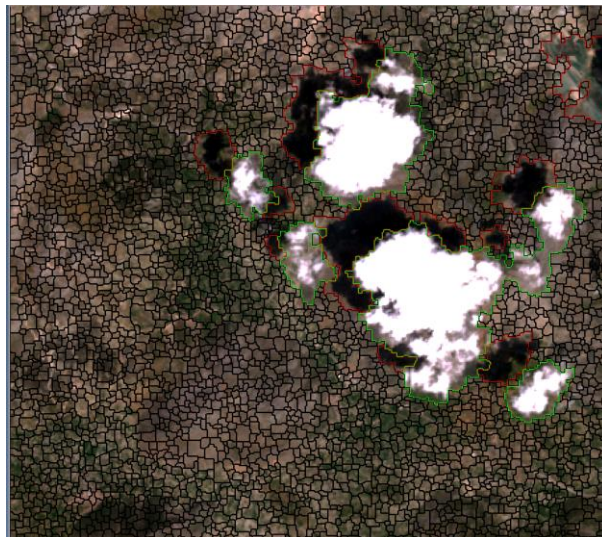


Figure 5.1 : Sample result of cloud and cloud shadow detection

Traditional cloud removal methods could be categorized into three methods: image filtering method, mathematical morphologic method and multitemporal cloud free areas composition (Zhengke et al, 2011).

Image filtering method aims to remove thin clouds (Feng et al, 2004). The limitation of image filtering method is that it can remove thin clouds from images but cannot recover information under cloud cover effectively, meanwhile, the filtering process decrease energy of image which cause radiometric loss. The mathematical morphologic strategy uses statistical test to predict pixel values under clouds and cloud shadows in reference scenes from multitemporal dataset (Helmer and Ruefenacht, 2005). Cloud-free areas cloning method uses multitemporal data which you can check

radiometric consistency and then can yield better results in case of radiometry (Wang, 1999; Gabarda and Cristobal 2007; Tseng, 2008). In this study, an automated cloud and cloud shadow removal method is proposed to generate cloud-free image. In which, cloud and cloud shadows are detected on basis of both spectral and spatial tests.

Lin et al, (2013) categorize reconstruction methods into three categories such as: inpainting, multispectral and multitemporal-based methods.

In inpainting-based methods, information of cloud covered regions is synthesized based on using the techniques of image synthesis and inpainting (Maalouf et al. 2009; Lorenzi et al. 2011). The inpainting-based methods can yield a visually good looking result that is suitable for cloud-free visualization purposes such as satellite image layer. However, inconsistency of radiometry makes the results unsuitable for detailed data analysis.

In multispectral-based methods, multispectral data are used in cloud detection and information reconstruction steps (Rakwatin 2009; Roy et al. 2008; Chun et al. 2004; Wang et al. 2005; Zhang et al. 2009). These methods, based on de-noising and intensity interpolation, can effectively reconstruct information with good results (Lin et al. 2013).

Multitemporal-based methods (Melgani 2006; Benabdelkader and Melgani 2008; USGS 2004; Gabarda and Cristobal 2007; Helmer and Ruefenacht 2005; Jiao et al. 2007; Wang et al. 1999; Tseng et al. 2008) compared with the inpainting and multispectral-based methods, which rely on both temporal and spatial relationships, shows better results with reconstruction of opaque cloud covered pixels. Melgani (2006) and Benabdelkader and Melgani (2008) developed a prediction method to find spectrotemporal relationships between the multitemporal images. The spectrotemporal relationships are calculated from cloud-free regions in the neighbourhood of cloud covered regions over the available multitemporal images. Li et al. (2013) also developed a threshold-based approach to identify the best cloud-free and non-shadow pixels of a given region. A cloud-free image is then generated by mosaicking the selected cloud-free pixels. While methods above can yield good results for homogenous regions, these methods based on data fusion can show difficulties with clouds over heterogeneous land cover. Lin et al. (2013) proposed an information cloning algorithm that selects cloud-free patches using a quality assessment index and

reconstruct patches by using a global optimization process. Thus, this method can yield good cloud-free results for opaque clouds (Lin et al. 2013).

In this study, cloud patches are cloned with cloudless satellite images from multitemporal dataset by using most correlated image for any cloud area (Figure 5.2). This study is an application of information reconstruction technique to cloudless images generation. General workflow of cloning method is given in Figure 5.3.



Figure 5.2 : Multitemporal dataset.

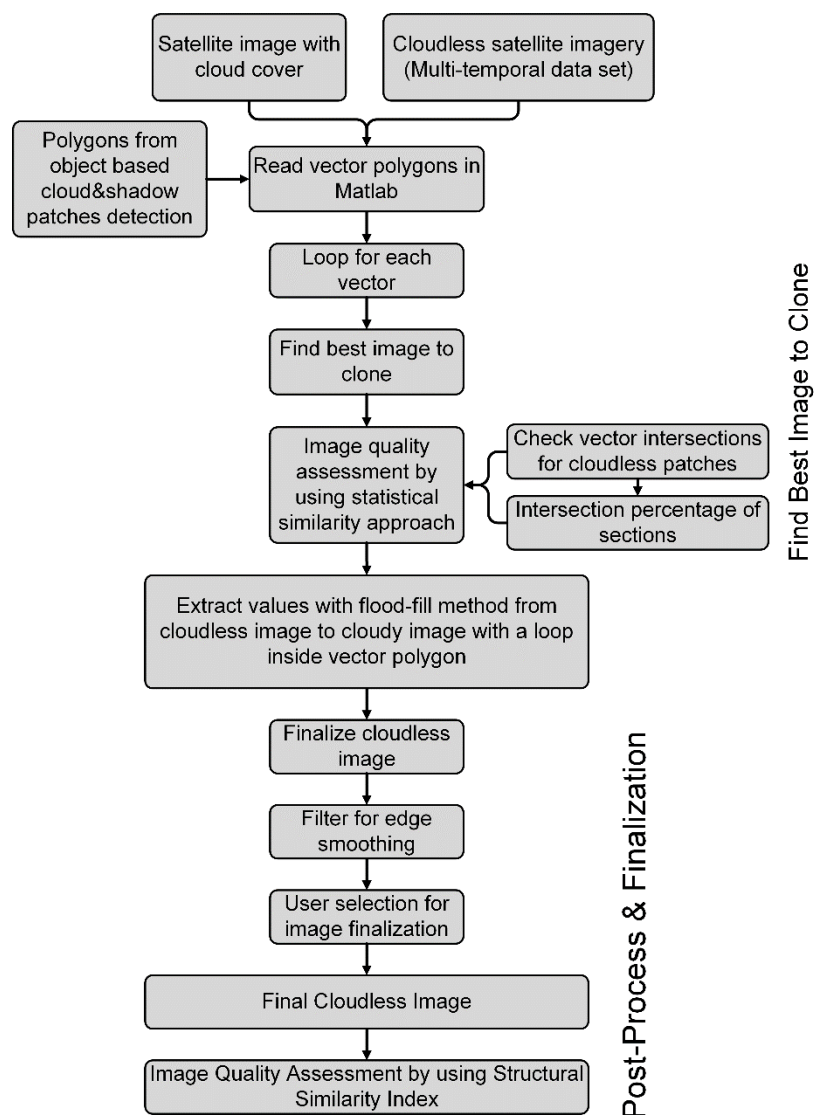


Figure 5.3 : Workflow of cloning procedure.

Replacing the cloud and shadow covered pixels with their corresponding cloud-free pixels and then adjusting the reflectance values of the replaced pixels has been proven

inappropriate the image radiometry change based on conditions of data acquisition (Lin et al. 2013). In addition, contrary to pixel-by-pixel information reconstruction (Melgani 2006, Benabdelkader and Melgani 2008), which may contain radiometric inconsistency, Lin et al. (2003) proposed a patch-based method. To address these problems, we propose a best image choosing algorithm to choose best cloudless image to clone by using seasonal and spectral similarity. Also superpixel segmentation algorithm helps to select suitable cloudless patches from a set of cloudless multitemporal dataset. Edge smoothing is also showing better seamless information reconstruction results. Also, results are evaluated by using image quality assessment metrics to check reliability. Proposed method can produce better cloud-free images in terms of radiometric accuracy and consistency compared to other cloud removal methods in previous studies. Visual flowchart of cloning process is given in Figure 5.4.

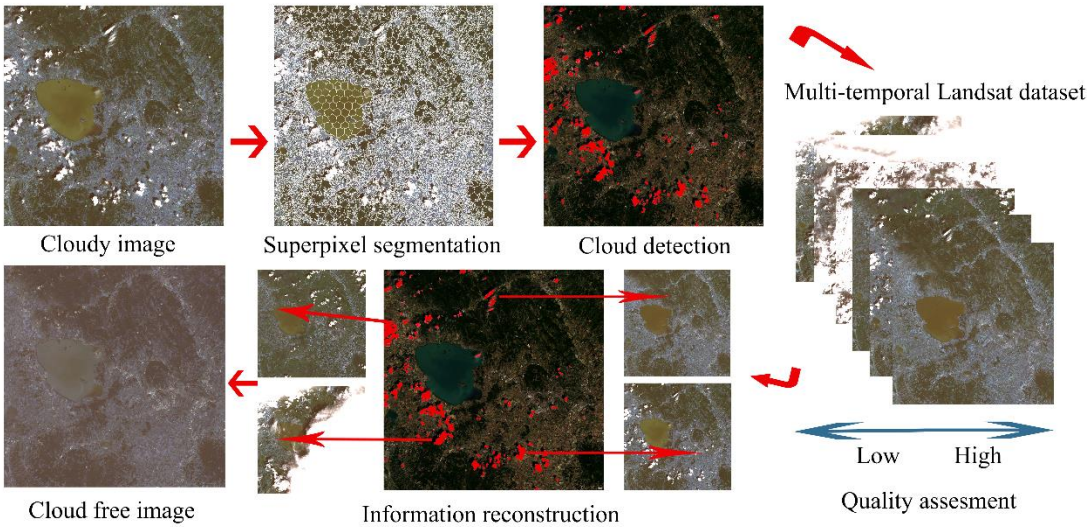


Figure 5.4 : Flowchart of cloud cloning method.

5.1 Choose Best Image to Clone

Achieving radiometric consistency is an important step for cloning process. In this study, image statistics, multitemporal image dataset and vector intersections are used to find best cloudless image to use in cloning process.

5.1.1 Image Correlation Approach

Correlation calculation between cloud image and multitemporal cloudless images is the main metric used to find choosing best image to clone different cloud patches (Figure 5.5). For each patches correlation between different images is calculated and image with maximum correlation is chosen (MathWorks, 2014) (equation 5.1). Two months of time interval is chosen to reduce radiometric inconsistency because of seasonal change if applicable.

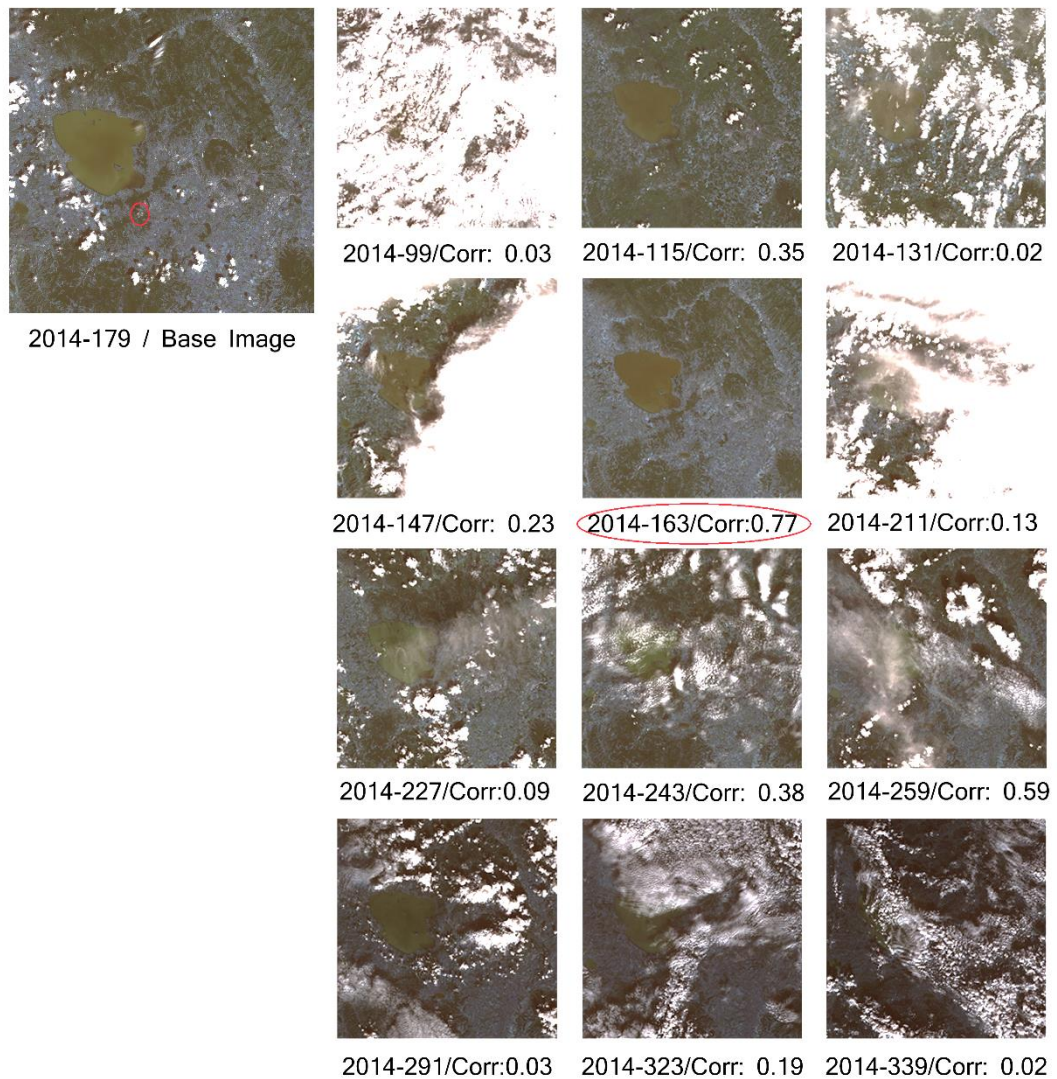


Figure 5.5 : Correlation calculations between images to choose best image to clone.

A, B image, r correlation coefficient, \bar{A} and \bar{B} mean of all pixels:

$$r = \frac{\sum_m \sum_n (A_{mn} - \bar{A})(B_{mn} - \bar{B})}{\sqrt{(\sum_m \sum_n (A_{mn} - \bar{A})^2)(\sum_m \sum_n (B_{mn} - \bar{B})^2)}} \quad (5.1)$$

5.1.2 Vector Intersection Approach

Figure 5.6 shows general concept of finding cloudless satellite image for each cloud patches. Radiometric similarity is the most important metric for choosing cloudless image from multitemporal dataset. Before this important step, for each cloud patches, checking multitemporal dataset for cloud covered pixels intersections is the key point for information reconstruction. Proposed algorithm is checking all multitemporal dataset for each cloud patch to find image without intersection to start cloning process (Figure 5.7). If there is not any image without intersection, intersection percentages are compared to each other by supporting image similarity to decide which image to choose (Figure 5.8-Figure 5.9).

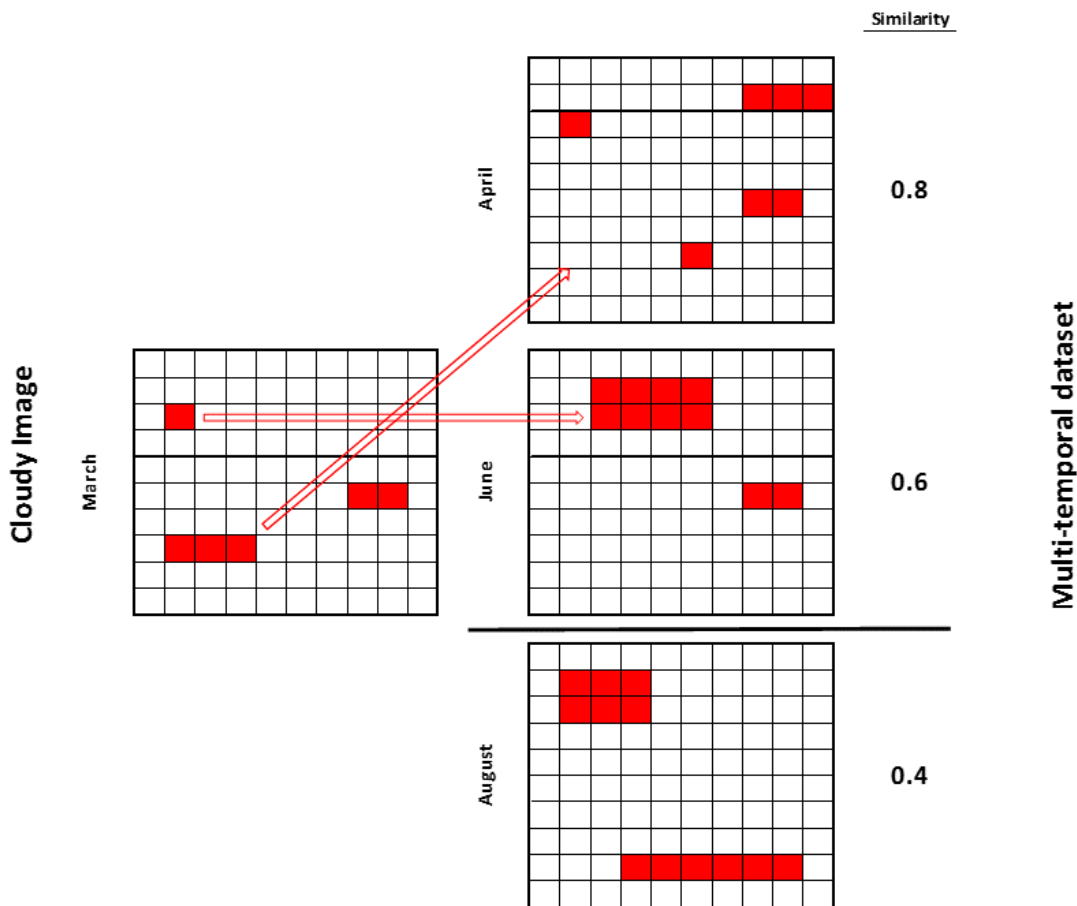


Figure 5.6 : Finding best cloudless image for cloud patches.

| | | | | | | | | | | | | | | |
|-----------|-----------|-----------|-----------|-----------|-----------|-----------|-----------|-----------|-----------|-----------|-----------|-----------|-----------|-----------|
| | shp1 vec1 | shp1 vec2 | shp1 vec3 | shp1 vec4 | shp2 vec1 | shp2 vec2 | shp3 vec1 | shp3 vec2 | shp3 vec3 | shp4 vec1 | shp4 vec2 | shp4 vec3 | shp5 vec1 | shp5 vec2 |
| shp1 vec1 | 0 | 0 | 0 | 0 | 0 | 0 | 0 | 0 | 1 | 0 | 0 | 0 | 0 | 1 |
| shp1 vec2 | 0 | 0 | 0 | 0 | 0 | 0 | 0 | 0 | 0 | 0 | 0 | 1 | 0 | 0 |
| shp1 vec3 | 0 | 0 | 0 | 0 | 0 | 0 | 0 | 0 | 0 | 0 | 1 | 0 | 0 | 0 |
| shp1 vec4 | 0 | 0 | 0 | 0 | 0 | 0 | 0 | 0 | 0 | 0 | 0 | 0 | 0 | 0 |
| shp2 vec1 | 0 | 0 | 0 | 0 | 0 | 0 | 0 | 0 | 0 | 0 | 0 | 0 | 1 | 0 |
| shp2 vec2 | 0 | 0 | 0 | 0 | 0 | 0 | 0 | 0 | 0 | 0 | 0 | 0 | 0 | 0 |
| shp3 vec1 | 0 | 0 | 0 | 0 | 0 | 0 | 0 | 0 | 0 | 0 | 0 | 0 | 0 | 0 |
| shp3 vec2 | 0 | 0 | 0 | 0 | 0 | 0 | 0 | 0 | 0 | 0 | 0 | 0 | 0 | 0 |
| shp3 vec3 | 1 | 0 | 0 | 0 | 0 | 0 | 0 | 0 | 0 | 0 | 0 | 0 | 0 | 1 |
| shp4 vec1 | 0 | 0 | 0 | 0 | 0 | 0 | 0 | 0 | 0 | 0 | 0 | 0 | 0 | 0 |
| shp4 vec2 | 0 | 0 | 1 | 0 | 0 | 0 | 0 | 0 | 0 | 0 | 0 | 0 | 0 | 0 |
| shp4 vec3 | 0 | 1 | 0 | 0 | 0 | 0 | 0 | 0 | 0 | 0 | 0 | 0 | 0 | 0 |
| shp5 vec1 | 0 | 0 | 0 | 0 | 1 | 0 | 0 | 0 | 0 | 0 | 0 | 0 | 0 | 0 |
| shp5 vec2 | 1 | 0 | 0 | 0 | 0 | 0 | 0 | 0 | 1 | 0 | 0 | 0 | 0 | 0 |

0: No intersection
1: Intersection

Figure 5.7 : Intersection check between cloud patches.

| Patch to Patch | Intersection Percentage |
|----------------|-------------------------|
| 1 1 3 3 | 0,289262108 |
| 1 1 5 2 | 0,134085008 |
| 1 2 4 3 | 0,06698818 |
| 1 3 4 2 | 0,047004757 |
| 1 4 3 2 | 1 |
| 3 2 1 4 | 0,176760908 |
| 3 3 1 1 | 0,403571137 |
| 3 3 5 2 | 0,114821778 |
| 4 2 1 3 | 0,306899626 |
| 4 3 1 2 | 0,326800818 |
| 5 2 1 1 | 0,480630952 |
| 5 2 3 3 | 0,29500354 |

Figure 5.8 : Intersection percentages of cloud patches with other cloud patches in multitemporal image dataset.

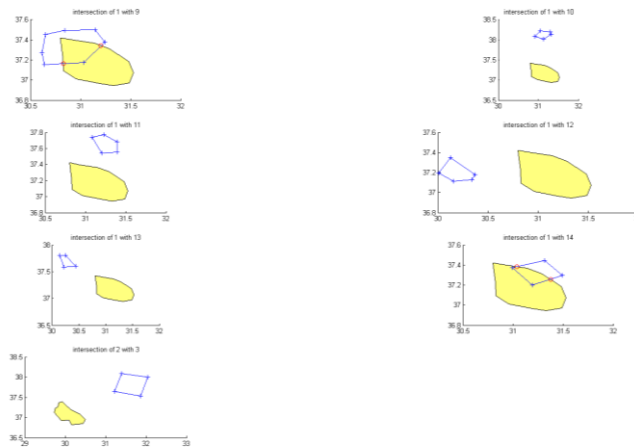


Figure 5.9 : Visual intersection rates of cloud patches.

5.2 Edge Smoothing for Seamless and Smooth Cloning

Flood Fill algorithm reconstructs pixel information from cloudless image to cloud image. While this information reconstruction process, edges of patches shows a translation effect. Creation of seamless cloudless image is one of the most important step of this study. Averaging filter (mean filter) is used to smooth edges of cloud patches to create a seamless effect (Figure 5.10, Figure 5.11).

| | | |
|---------------|---------------|---------------|
| $\frac{1}{9}$ | $\frac{1}{9}$ | $\frac{1}{9}$ |
| $\frac{1}{9}$ | $\frac{1}{9}$ | $\frac{1}{9}$ |
| $\frac{1}{9}$ | $\frac{1}{9}$ | $\frac{1}{9}$ |

Figure 5.10 : Averaging filter.

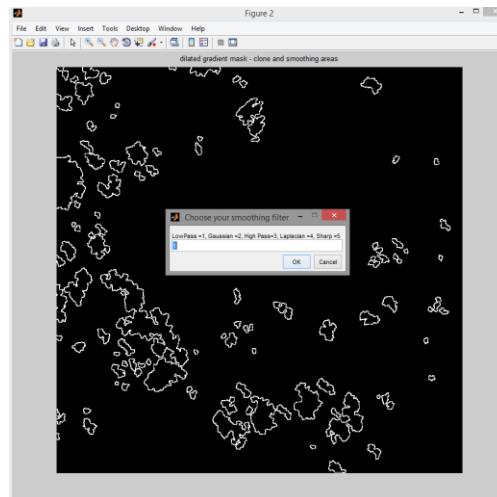


Figure 5.11 : Edges of cloud patches which are applied edge smoothing with averaging filter.

5.3 Flood Fill for Multitemporal Image Cloning

Flood fill is an algorithm that finds connected areas of a given node in a multi-dimensional array. Games such as Go and Minesweeper are using this algorithm for finding which pieces are cleared and paint programs are using it for bucket tool to fill areas with different color. In this study, after checking cloud patches intersections and image similarity calculations, suitable pixels from cloudless image are cloned to cloud image pixels by using Flood Fill algorithm by processing pixel-by-pixel. Sample results from image cloning process is given in Figure 5.12.

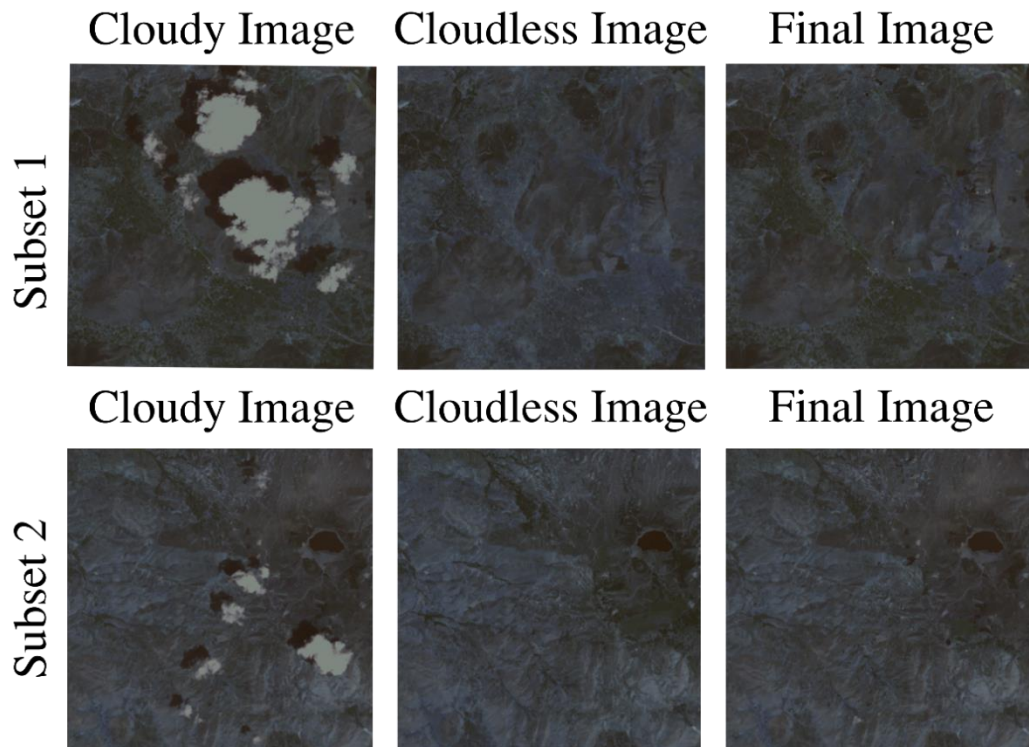


Figure 5.12 : Cloning results after information reconstruction by using Flood Fill method.

5.4 Cloning Results and Image Quality Tests

Evaluation of cloning accuracy is a difficult process. Scene spectral variance similarity of cloudless cloning final image to cloud image is the main metric to evaluate success of cloning process. Structural Similarity Index (SSIM) is used to check similarity of final cloudless image with original cloud image. SSIM is designed to improve traditional methods such as peak signal-to-noise ratio (PSNR) and mean squared error (MSE), which have proven to be inconsistent with human visual perception (Wang et al, 2004). SSIM is one of the most used image quality metric which is used for measuring similarity between two images. One image is accepted as a base image and other image is compared to base image in this method. Not only contrast and spectral signature but also structural similarity is tested in this method. SSIM is chosen as a suitable quality metric because of this specifications.

The SSIM formula is based on three comparison measurements between the samples of x and y: luminance (l), contrast (c) and structure (s) which yield to compare two images by using spectral and structural specifications (equation 5.2). (Brunet et al, 2012)(Wang et al, 2003). SSIM is tested and compared to state-of-art Root Mean

Square Error (RMSE) with different processed images in Figure 5.13 and Figure 5.14 to check efficiency.

$$SSIM(x, y) = [I(x, y)]^\alpha \cdot [c(x, y)]^\beta \cdot [s(x, y)]^\gamma \quad (5.2)$$



Figure 5.13 : SSIM & RMSE results a) Original b) Histogram equalized c) Contrast adjusted d) Salt & Pepper effect e) Blurred f) JPEG converted.

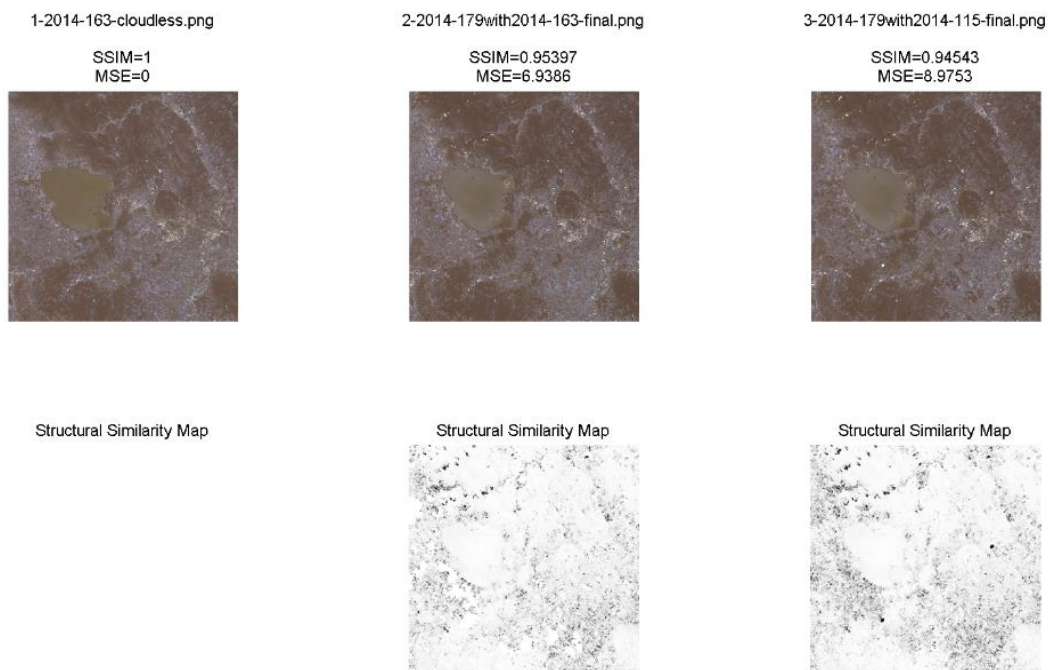


Figure 5.14 : SSIM results and similarity maps of two different cloning results.

Cloudless images are important for all passive remote sensing applications. There are many studies conducted in this topic of remote sensing. Although some spectral

methods are developed to remove haze effects, removing oblique clouds from satellite image is a difficult process. Using multitemporal image dataset to remove or clone oblique clouds is the most applicable method for cloning oblique clouds. In this study, cloning of cloud image is completed with information reconstruction from cloudless multitemporal dataset of the same area with different acquisition dates. Accurate patch determination is the main step for cloning process which is the main step of seamless cloning result. Superpixel classification approach which is used to detect both clouds and shadows is provided better patch determination for detection of cloning edges. Conservation of spectral and structural consistency is the main aim of our proposed cloning algorithm. Different image quality and image similarity metrics are tested and implemented to preserve both spectral and structural information while cloning process. Transferability of proposed method is also tested by using different satellite images from various study areas by using satellite images with different acquisition dates.

6. RESULTS AND DISCUSSION

Detection and cloning of cloud and shadow regions is a popular study area in remote sensing for a long time, and lots of methods have been developed. Spectral methods gives satisfactory results for removing haze effects from satellite images. Processing opaque clouds by using spectral methods is not sufficient remove clouds and create a cloudless satellite image by itself. Information reconstruction concept applied to cloud images gives sufficient results for creating cloudless images from multitemporal image dataset. These methods provide sufficient accuracy in many cases. Nevertheless, they don't provide enough accuracy for some specific cases such as opaque clouds over heterogeneous regions. Beside pixel-based methods, segmentation-based methods which groups pixels into superpixels are a new study area for detection of clouds and shadows. By separating image into homogeneous pixel groups, not only computational workload can be decreased but also features can be obtained on the image effectively regarding geometrical characteristics by the help of object-based classification approach. Methods developed in this study is based on segmentation approach for cloud and shadow detection. Classification results is directly related to accuracy of superpixels created in the pre-processing step of classification. Accuracy of cloud identification process is the main input of cloning process to create cloudless images from cloud images. For this reason, region size is chosen as small as possible to decrease the size of superpixels to minimize feature loss while pixel grouping process. Spectral characteristics of features such as cloud and shadow in images are significant in terms of brightness and darkness. In the light of this information, cloud and shadow areas are grouped into superpixels by using SLIC segmentation algorithm. Segmentation-based approach which uses both spectral and spatial information to group pixels provides more successful results compared to pixel-based method in this study. Clouds and shadows are detected from the image, by creating indices developed within spectral tests by adding different parameters to the multi-criteria rule set such as: brightness temperature, sun azimuth, NDSI and NDWI. Shadow classification

accuracy is increased with the help of cloud-shadow projection approach as a new solution to this problem which uses the geometrical relation between cloud and shadow. Cloud and shadow classification results are compared to Fmask method. Although, both methods have sufficient recall rates for cloud and shadow classification, region growing rate used by Fmask method to increase confidence interval causes non-cloud and non-shadow areas classified as cloud and shadow on many regions. Testing our algorithm with other satellites is also possible, if satellites have thermal and infrared bands. One of the restrictions of the proposed algorithm is the necessity of thermal infrared bands to find cold regions to compare clouds with other cold regions. Using only visible bands to find cloud regions is not possible in our algorithm, but using techniques like deep learning can yield good results with three bands images. Transferability of this method is tested with the same parameters by using different images from different study areas. In addition to algorithm like ACCA and Fmask, the usability and transferability of the algorithm developed here is proven in terms of simplification of processing steps and decreasing computational workload because of its superpixel-based approach.

Cloning cloud patches from cloudless multitemporal dataset is the information reconstruction concept for this study. Superpixel segmentation detects cloud patches accurately to start Flood Fill process to reconstruct cloudless information for cloud patches. Choosing best image for cloning process is an important step to conserve spectral consistency. Patch by patch correlations calculations between multitemporal dataset are used to find best image for cloning in terms of spectral consistency. Vector intersection calculations are also used to find best cloudless dataset for cloning process to achieve full cloudless patch cloning. Information reconstruction from cloudless image to cloud image is implemented by using Flood Fill algorithm by pixel-by-pixel which is one of the most known graphical filling algorithm used in graphical applications. Conservation of spectral and structural consistency is the main aim of our proposed cloning algorithm. SSIM is used to evaluate accuracy of cloning in terms of spectral and structural consistency with cloudless reference image. Transferability of proposed method is also tested by using different satellite images from various study areas by using satellite images with different acquisition dates. Accurate detection of cloud and shadow patches for cloning process is most important step. Information reconstruction for cloud images by our proposed method gives sufficient results for

passive remote sensing applications which are interrupted by clouds. Method developed within this study can yield continuity for analyses such as time series and NDVI calculations.

REFERENCES

- Achanta, R., Shaji, A., Smith, K., Lucchi, A., Fua, P., & Ssstrunk, S.** (2012). SLIC Superpixels Compared to State-of-the-Art Superpixel Methods. *IEEE Transactions on Pattern Analysis and Machine Intelligence*, *34*(11), 2274–2282. <https://doi.org/10.1109/TPAMI.2012.120>
- Amato, U., Antoniadis, A., Cuomo, V., Cuttillo, L., Franzese, M., Murino, L., & Serio, C.** (2008). Statistical cloud detection from SEVIRI multispectral images. *Remote Sensing of Environment*, *112*(3), 750–766. <https://doi.org/10.1016/j.rse.2007.06.004>
- Amazon.** (2015). Landsat on AWS. Retrieved December 10, 2015, from <https://aws.amazon.com/public-data-sets/landsat/>
- Arvidson, T., Gasch, J., & Goward, S. N.** (2001). Landsat 7’s long-term acquisition plan — an innovative approach to building a global imagery archive. *Remote Sensing of Environment*, *78*(1–2), 13–26. [https://doi.org/10.1016/S0034-4257\(01\)00263-2](https://doi.org/10.1016/S0034-4257(01)00263-2)
- Benabdelkader, S., and Melgani, F.** (2008). Contextual Spatiospectral Postreconstruction of Cloud-Contaminated Images. *IEEE Geoscience and Remote Sensing Letters*, *5*(2), 204–208. <https://doi.org/10.1109/LGRS.2008.915596>
- Berendes, T., Sengupta, S. K., Welch, R. M., Wielicki, B. A., & Navar, M.** (1992). Cumulus cloud base height estimation from high spatial resolution Landsat data: a Hough transform approach. *IEEE Transactions on Geoscience and Remote Sensing*, *30*(3), 430–443. <https://doi.org/10.1109/36.142921>
- Birch, P.** (2016). Powering geospatial analysis: public geo datasets now on Google Cloud. Retrieved November 10, 2016, from <https://cloud.google.com/storage/docs/public-datasets/landsat>
- Braaten, J. D., Cohen, W. B., & Yang, Z.** (2015). Automated cloud and cloud shadow identification in Landsat MSS imagery for temperate ecosystems. *Remote Sensing of Environment*, *169*, 128–138. <https://doi.org/10.1016/j.rse.2015.08.006>
- Brunet, D., Vrscay, E. R., & Zhou Wang.** (2012). On the Mathematical Properties of the Structural Similarity Index. *IEEE Transactions on Image Processing*, *21*(4), 1488–1499. <https://doi.org/10.1109/TIP.2011.2173206>
- Chavez, P. S.** (1996). Image-based atmospheric corrections - Revisited and improved (Review). *Photogrammetric Engineering and Remote Sensing*, *62*(9), 1025–1036.

- CIMSS.** (2016). Cloud Identification in Course of Satellite Meteorology. Retrieved from https://cimss.ssec.wisc.edu/satmet/modules/4_clouds/clouds-1.html
- Feng, C., Ma, J., Dai, Q., & Xue Chen.** (2004). An improved method for cloud removal in ASTER data change detection. In *IEEE International IEEE International Geoscience and Remote Sensing Symposium, 2004. IGARSS '04. Proceedings. 2004 (Vol. 5, pp. 3387–3389)*. IEEE. <https://doi.org/10.1109/IGARSS.2004.1370431>
- Congedo, L.** (2016). Semi-Automatic Classification Plugin Documentation. Release 5.0.2.1.
- Gabarda, S., and Cristóbal, G.** (2007). Cloud covering denoising through image fusion. *Image and Vision Computing*, 25(5), 523–530. <https://doi.org/10.1016/j.imavis.2006.03.007>
- Gao, B.** (1996). NDWI—A normalized difference water index for remote sensing of vegetation liquid water from space. *Remote Sensing of Environment*, 58(3), 257–266. [https://doi.org/10.1016/S0034-4257\(96\)00067-3](https://doi.org/10.1016/S0034-4257(96)00067-3)
- Gao, B.-C., and Kaufman, Y. J.** (1995). Selection of the 1.375- μm MODIS Channel for Remote Sensing of Cirrus Clouds and Stratospheric Aerosols from Space. *Journal of the Atmospheric Sciences*, 52(23), 4231–4237. [https://doi.org/10.1175/1520-0469\(1995\)052<4231:SOTMCF>2.0.CO;2](https://doi.org/10.1175/1520-0469(1995)052<4231:SOTMCF>2.0.CO;2)
- Gao, B.-C., Kaufman, Y. J., Han, W., & Wiscombe, W. J.** (1998). Corection of thin cirrus path radiances in the 0.4-1.0 μm spectral region using the sensitive 1.375 μm cirrus detecting channel. *Journal of Geophysical Research: Atmospheres*, 103(D24), 32169–32176. <https://doi.org/10.1029/98JD02006>
- Gao, B.-C., Yang, P., Han, W., Li, R.-R., & Wiscombe, W. J.** (2002). An algorithm using visible and 1.38- μm channels to retrieve cirrus cloud reflectances from aircraft and satellite data. *IEEE Transactions on Geoscience and Remote Sensing*, 40(8), 1659–1668. <https://doi.org/10.1109/TGRS.2002.802454>
- GESDISC.** (2016). Brightness Temperature. Retrieved from http://disc.sci.gsfc.nasa.gov/data-holdings/PIP/brightness_temperature.shtml
- Gundersen, E.** (2013). Cloudless Atlas with Landsat. Retrieved from <https://www.mapbox.com/blog/cloudless-atlas-with-landsat/>
- Hall, D. K., and Riggs, G. A.** (2011). Normalized-Difference Snow Index (NDSI). In *Encyclopedia of Snow, Ice and Glaciers* (pp. 779–780). https://doi.org/10.1007/978-90-481-2642-2_376
- Hancher, M.** (2016). Only clear skies on Google Maps and Earth. Retrieved June 6, 2014, from <https://googleblog.blogspot.com.tr/2013/06/only-clear-skies-on-google-maps-and.html>
- Helmer, E., and Rufenacht, B.** (2005). Cloud-Free Satellite Image Mosaics with Regression Trees and Histogram Matching. *Photogrammetric Engineering and Remote Sensing*, 71(9), 1079–1089.

- Ho, A. T. S., and Cai, Z.** (1996). Cloud detection in satellite images for tropical regions. In B. Huberty, J. B. Lurie, J. A. Caylor, P. Coppin, & P. C. Robert (Eds.), *Multispectral Imaging for Terrestrial Applications* (p. 167). <https://doi.org/10.1117/12.256091>
- Huang, C., Thomas, N., Goward, S. N., Masek, J. G., Zhu, Z., Townshend, J. R. G., & Vogelmann, J. E.** (2010). Automated masking of cloud and cloud shadow for forest change analysis using Landsat images. *International Journal of Remote Sensing*, *31*(20), 5449–5464. <https://doi.org/10.1080/01431160903369642>
- Hughes, M., and Hayes, D.** (2014). Automated Detection of Cloud and Cloud Shadow in Single-Date Landsat Imagery Using Neural Networks and Spatial Post-Processing. *Remote Sensing*, *6*(6), 4907–4926. <https://doi.org/10.3390/rs6064907>
- Hutchison, K. D., Mahoney, R. L., Vermote, E. F., Kopp, T. J., Jackson, J. M., Sei, A., & Iisager, B. D.** (2009). A Geometry-Based Approach to Identifying Cloud Shadows in the VIIRS Cloud Mask Algorithm for NPOESS. *Journal of Atmospheric and Oceanic Technology*, *26*(7), 1388–1397. <https://doi.org/10.1175/2009JTECHA1198.1>
- Irish, R. R.** (2000). Landsat 7 automatic cloud cover assessment. In S. S. Shen & M. R. Descour (Eds.), *Proc. SPIE 4049, Algorithms for Multispectral, Hyperspectral, and Ultraspectral Imagery VI* (p. 348). <https://doi.org/10.1117/12.410358>
- Irish, R. R., Barker, J. L., Goward, S. N., & Arvidson, T.** (2006). Characterization of the Landsat-7 ETM+ Automated Cloud-Cover Assessment (ACCA) Algorithm. *Photogrammetric Engineering & Remote Sensing*, *72*(10), 1179–1188. <https://doi.org/10.14358/PERS.72.10.1179>
- Jiao, Q., Luo, W., Liu, X., & Zhang, B.** (2007). Information reconstruction in the cloud removing area based on multitemporal CHRIS images. In Y. Wang, J. Li, B. Lei, & J. Yang (Eds.), *MIPPR 2007: Remote Sensing and GIS Data Processing and Applications; and Innovative Multispectral Technology and Applications* (p. 679029). <https://doi.org/10.1117/12.750462>
- Ju, J., and Roy, D. P.** (2008). The availability of cloud-free Landsat ETM+ data over the conterminous United States and globally. *Remote Sensing of Environment*, *112*(3), 1196–1211. <https://doi.org/10.1016/j.rse.2007.08.011>
- Le Hégarat-Masclé, S., and André, C.** (2009). Use of Markov Random Fields for automatic cloud/shadow detection on high resolution optical images. *ISPRS Journal of Photogrammetry and Remote Sensing*, *64*(4), 351–366. <https://doi.org/10.1016/j.isprsjprs.2008.12.007>
- Li, M., Liew, S. C., & Kwoh, L. K.** (2003). Producing cloud free and cloud-shadow free mosaic from cloudy IKONOS images. In IGARSS 2003. 2003 *IEEE International Geoscience and Remote Sensing Symposium. Proceedings* (IEEE Cat. No.03CH37477) (Vol. 6, pp. 3946–3948). IEEE. <https://doi.org/10.1109/IGARSS.2003.1295323>

- Lillesand, T., and Kiefer, R. W.** (2002). *Remote Sensing and Image Interpretation* (4th ed.). John Wiley and Sons.
- Lin, C.-H., Lai, K.-H., Chen, Z.-B., & Chen, J.-Y.** (2014). Patch-Based Information Reconstruction of Cloud-Contaminated Multitemporal Images. *IEEE Transactions on Geoscience and Remote Sensing*, 52(1), 163–174. <https://doi.org/10.1109/TGRS.2012.2237408>
- Lin, C.-H., Tsai, P.-H., Lai, K.-H., & Chen, J.-Y.** (2013). Cloud Removal From Multitemporal Satellite Images Using Information Cloning. *IEEE Transactions on Geoscience and Remote Sensing*, 51(1), 232–241. <https://doi.org/10.1109/TGRS.2012.2197682>
- Lloyd, S.** (1982). Least squares quantization in PCM. *IEEE Transactions on Information Theory*, 28(2), 129–137. <https://doi.org/10.1109/TIT.1982.1056489>
- Lorenzi, L., Melgani, F., & Mercier, G.** (2011). Inpainting Strategies for Reconstruction of Missing Data in VHR Images. *IEEE Geoscience and Remote Sensing Letters*, 8(5), 914–918. <https://doi.org/10.1109/LGRS.2011.2141112>
- Loyd, C.** (2012). Cloudless atlas. Retrieved November 2, 2016, from <https://www.flickr.com/photos/vruba/>
- Luo, Y., Trishghenko, A., & Khlopenkov, K.** (2008). Developing clear-sky, cloud and cloud shadow mask for producing clear-sky composites at 250-meter spatial resolution for the seven MODIS land bands over Canada and North America. *Remote Sensing of Environment*, 112(12), 4167–4185. <https://doi.org/10.1016/j.rse.2008.06.010>
- Maalouf, A., Carre, P., Augereau, B., & Fernandez-Maloigne, C.** (2009). A Bandelet-Based Inpainting Technique for Clouds Removal From Remotely Sensed Images. *IEEE Transactions on Geoscience and Remote Sensing*, 47(7), 2363–2371. <https://doi.org/10.1109/TGRS.2008.2010454>
- MathWorks, I.** (2014). Corr2, 2-D Correlation Coefficient. Retrieved from <http://www.mathworks.com/help/images/ref/corr2.html>
- Melgani, F.** (2006). Contextual reconstruction of cloud-contaminated multitemporal multispectral images. *IEEE Transactions on Geoscience and Remote Sensing*, 44(2), 442–455. <https://doi.org/10.1109/TGRS.2005.861929>
- Moran, M. S., Jackson, R. D., Slater, P. N., & Teillet, P. M.** (1992). Evaluation of simplified procedures for retrieval of land surface reflectance factors from satellite sensor output. *Remote Sensing of Environment*, 41(2–3), 169–184. [https://doi.org/10.1016/0034-4257\(92\)90076-V](https://doi.org/10.1016/0034-4257(92)90076-V)
- Muller, B.** (2016). Detecting Cloud Type in Satellite Imagery. Retrieved October 9, 2016, from <http://wx.db.erau.edu/faculty/mullerb/>
- Rakwatin, P., Takeuchi, W., & Yasuoka, Y.** (2009). Restoration of Aqua MODIS Band 6 Using Histogram Matching and Local Least Squares Fitting. *IEEE Transactions on Geoscience and Remote Sensing*, 47(2), 613–627. <https://doi.org/10.1109/TGRS.2008.2003436>

- Roy, D. P., Ju, J., Lewis, P., Schaaf, C., Gao, F., Hansen, M., & Lindquist, E.** (2008). Multi-temporal MODIS–Landsat data fusion for relative radiometric normalization, gap filling, and prediction of Landsat data. *Remote Sensing of Environment*, 112(6), 3112–3130. <https://doi.org/10.1016/j.rse.2008.03.009>
- Saunders, R. W., and Kriebel, K. T.** (1988). An improved method for detecting clear sky and cloudy radiances from AVHRR data. *International Journal of Remote Sensing*, 9(1), 123–150. <https://doi.org/10.1080/01431168808954841>
- Simpson, J.** (1995). Improved cloud detection in GOES scenes over the oceans. *Remote Sensing of Environment*, 52(2), 79–94. [https://doi.org/10.1016/0034-4257\(95\)00036-Z](https://doi.org/10.1016/0034-4257(95)00036-Z)
- Simpson, J. J., and Stitt, J. R.** (1998). A procedure for the detection and removal of cloud shadow from AVHRR data over land. *IEEE Transactions on Geoscience and Remote Sensing*, 36(3), 880–897. <https://doi.org/10.1109/36.673680>
- Simpson, J. J., Zhonghai Jin, & Stitt, J. R.** (2000). Cloud shadow detection under arbitrary viewing and illumination conditions. *IEEE Transactions on Geoscience and Remote Sensing*, 38(2), 972–976. <https://doi.org/10.1109/36.841979>
- Sobrino, J. A., Jiménez-Muñoz, J. C., & Paolini, L.** (2004). Land surface temperature retrieval from LANDSAT TM 5. *Remote Sensing of Environment*, 90(4), 434–440. <https://doi.org/10.1016/j.rse.2004.02.003>
- Tseng, D.-C., Tseng, H.-T., & Chien, C.-L.** (2008). Automatic cloud removal from multi-temporal SPOT images. *Applied Mathematics and Computation*, 205(2), 584–600. <https://doi.org/10.1016/j.amc.2008.05.050>
- USGS** (2004). SLC-off Gap-Filled Products Gap-Fill Algorithm Methodology. Retrieved from <http://landsat.usgs.gov/documents/L7SLCGapFilledMethod.pdf>
- USGS** (2015). Landsat 8 (L8) Data Users Handbook. USGS.
- Url-1** <<https://www.wired.com/2013/05/a-cloudless-atlas/>>, date retrieved 10.01.2017.
- Vedaldi, A., and Fulkerson, B.** (2010). Vlfeat. In *Proceedings of the international conference on Multimedia - MM '10* (p. 1469). New York, New York, USA: ACM Press. <https://doi.org/10.1145/1873951.1874249>
- Wang, B., Ono, A., Muramatsu, K., Fujiwara, N., Bin, W., Atsuo, O. N. O., ... Fujiwara, N.** (1999). Automated Detection and Removal of Clouds and Their Shadows from Landsat TM Images. *IEICE Transactions on Information and Systems*, 82(2), 453–460. article.
- Wang, Z., Bovik, A. C., Sheikh, H. R., & Simoncelli, E. P.** (2004). Image Quality Assessment: From Error Visibility to Structural Similarity. *IEEE Transactions on Image Processing*, 13(4), 600–612. <https://doi.org/10.1109/TIP.2003.819861>

- Wang, Z., Simoncelli, E. P., & Bovik, A. C.** (2003). Multiscale structural similarity for image quality assessment. In *The Thirty-Seventh Asilomar Conference on Signals, Systems & Computers*, 2003 (pp. 1398–1402). IEEE. <https://doi.org/10.1109/ACSSC.2003.1292216>
- Wang, Z., Jin, J., Liang, J., Yan, K., & Peng, Q.** (2005). A new cloud removal algorithm for multi-spectral images. In L. Zhang, J. Zhang, & M. Liao (Eds.), *MIPPR 2005: SAR and Multispectral Image Processing* (p. 60430W). <https://doi.org/10.1117/12.654869>
- Wikipedia** (2016). Flood-fill. Retrieved October 22, 2016, from https://en.wikipedia.org/wiki/Flood_fill
- Zhang, C., Li, W., & Travis, D. J.** (2009). Restoration of clouded pixels in multispectral remotely sensed imagery with cokriging. *International Journal of Remote Sensing*, 30(9), 2173–2195. <https://doi.org/10.1080/01431160802549294>
- Zhang, X., Qin, F., & Qin, Y.** (2010). Study on the Thick Cloud Removal Method Based on Multi-Temporal Remote Sensing Images. In *2010 International Conference on Multimedia Technology* (pp. 1–3). IEEE. <https://doi.org/10.1109/ICMULT.2010.5631017>
- Zhengke, G., Fu, C., Jin, Y., Xinpeng, L., Fangjun, L., & Zhao Jing.** (2011). Automatic cloud and cloud shadow removal method for landsat TM images. In *IEEE 2011 10th International Conference on Electronic Measurement & Instruments* (pp. 80–84). IEEE. <https://doi.org/10.1109/ICEMI.2011.6037860>
- Zhu, Z., and Woodcock, C. E.** (2012). Object-based cloud and cloud shadow detection in Landsat imagery. *Remote Sensing of Environment*, 118, 83–94. <https://doi.org/10.1016/j.rse.2011.10.028>

CURRICULUM VITAE



Name Surname : Kaan KALKAN
Place and Date of Birth : Kadıköy, 26.10.1986
E-Mail : kaankalkan@gmail.com

EDUCATION :

- **B.Sc.** : 2009, Istanbul Technical University, Faculty of Civil Engineering, Department of Geomatics Engineering
- **M.Sc.** : 2011, Istanbul Technical University, Graduate School of Science Engineering and Technology, Department of Geomatics Engineering

PROFESSIONAL EXPERIENCE AND REWARDS:

- 2009-2012 Project Assistant at TÜBİTAK
- 2010-2014 Research Assistant at Istanbul Technical University, Department of Geomatics Engineering, Remote Sensing Division
- 2014-2016 Software Development Engineer at Havelsan, Image Processing Group
- 2016-.. Senior Researcher at TÜBİTAK Space Technologies Research Institute

PUBLICATIONS, PRESENTATIONS AND PATENTS ON THE THESIS:

- **Kalkan, K.**, & Maktav, D., 2016. Segmentation Based Cloud and Cloud Shadow Detection in Satellite Imagery. *Journal of Aeronautics and Space Technologies*.

OTHER PUBLICATIONS, PRESENTATIONS AND PATENTS:

- Akar, I., **Kalkan, K.**, Maktav, D., & Ozdemir, Y., 2009. Determination of land use effects on flood risk by using integration of GIS and remote sensing. 2009 4th International Conference on Recent Advances in Space Technologies (pp. 23–26). İstanbul, Turkey: IEEE.

- Arslan, A. E., & **Kalkan, K.**, 2013. Comparison of working efficiency of terrestrial laser scanner in day and night conditions. *ISPRS - International Archives of the Photogrammetry, Remote Sensing and Spatial Information Sciences*, XL-7/W2, 19–21.
- Carsten, J., Wolf, N., Thunig, H., Siegmund, A., Maktav, D., Sunar, F., Eşbah, H., Levent, T., Uysal, C., **Kalkan, K.**, Mercan, O., Akar, İ., 2011. Extraction and Multi-criteria Evaluation of Potential Space for Inner-Urban Development by Means of Optical VHR Satellite Imagery. *Proceedings of GTC 2011*, Geomatics Technologies in the City. Jeddah, Saudi Arabia.
- Çelik, B., & **Kalkan, K.**, 2012. Isıl Uzaktan Algılama Verileri Yardımıyla Yeryüzü Sıcaklıklarının Tespitinde Farklı Tek-Kanal Algoritmalarının Meteorolojik İstasyon Verileri Kullanılarak Karşılaştırılması: İstanbul Örneği. *IV. Uzaktan Algılama ve Coğrafi Bilgi Sistemleri Sempozyumu*. Zonguldak, Türkiye.
- Filiz, G., Maktav, D., **Kalkan, K.**, & Özer, O., 2013. Mobil Platformlar Üzerinden Gerçek Zamanlı Ekip Takip Sistemi. *TMMOB Coğrafi Bilgi Sistemleri Kongresi 2013*. Ankara, Türkiye.
- **Kalkan, K.**, & Akar, İ., 2010. Effects of Human Activities on Flood Risk and Recommendations for Prevention by Help of GIS and Remote Sensing. *TIEMS 7th Workshop*. Split, Croatia.
- **Kalkan, K.**, Bayram, B., Maktav, D., & Sunar, F., 2013. Comparison of support vector machine and object based classification methods for coastline detection. *ISPRS - International Archives of the Photogrammetry, Remote Sensing and Spatial Information Sciences*, XL-7/W2, 125–127.
- **Kalkan, K.**, Maktav, D., Özer, O., & Ceylan, S. 2012. Açık Kaynak Kodlu Veri Tabanı ve Harita Görselleştirme Arayüzleri Kullanarak Farklı Mekansal Verilerin Web Ortamında Görselleştirilmesi. *IV. Uzaktan Algılama ve Coğrafi Bilgi Sistemleri Sempozyumu*. Zonguldak, Türkiye.
- **Kalkan, K.**, Mercan, O. Y., & Maktav, D., 2010. Kıyı Çizgisinin Otomatik Olarak Belirlenmesi ve Coğrafi Bilgi Sistemleri ile Entegrasyonu (Matlab Uygulaması). *III. Uzaktan Algılama ve Coğrafi Bilgi Sistemleri Sempozyumu*. Kocaeli, Türkiye.
- Maktav, D., Jurgens, C., Siegmund, A., Sunar, F., Eşbah, H., **Kalkan, K.**, Uysal, C., Mercan, O., Akar, İ., Thunig, H., Wolf, N., 2011. Multi-criteria spatial decision support system for valuation of open spaces for urban planning. *Proceedings of 5th International Conference on Recent Advances in Space Technologies - RAST2011* (pp. 160–163). İstanbul, Turkey: IEEE.
- Maktav, D., Siegmund, A., Carsten, J., Naumann, S., Sunar, F., Eşbah, H., Levent, T., Uysal, C., **Kalkan, K.**, Mercan, O., Wolf, N., Thunig, H., 2010. Kentsel Gelişim için Potansiyel Alanların Uzaktan Algılama ve CBS ile Belirlenmesi ve Değerlemesi. *III. Uzaktan Algılama ve Coğrafi Bilgi Sistemleri Sempozyumu*. Kocaeli, Türkiye.
- Özkan, C., Osmanoğlu, B., Sunar, F., Staples, G., **Kalkan, K.**, & Balık Sanlı, F., 2012. Testing the Generalization Efficiency of Oil Slick Classification Algorithm using Multiple SAR Data for Deepwater Horizon Oil Spill. *ISPRS - International Archives of the Photogrammetry, Remote Sensing and Spatial Information Sciences*, XXXIX-B7, 67–72.

- **Kalkan, K.,** & Maktav, D., 2016. Segmentation Based Cloud and Cloud Shadow Detection in Satellite Imagery. *Journal of Aeronautics and Space Technologies.*
- **Kalkan, K.,** & Maktav, D., 2016. Çok Zamanlı Uydu Görüntülerinde Bulut-Gölge Alanlarının Klonlanması. *VI. Uzaktan Algılama ve Coğrafi Bilgi Sistemleri Sempozyumu.*
- **Kalkan, K.,** & Maktav, D., 2016. Landsat-8 Görüntülerinden Gölge ve Bulut Belirleme. *VI. Uzaktan Algılama ve Coğrafi Bilgi Sistemleri Sempozyumu.*
- Teke, M., Deveci, S., Öztoprak, F., Efendioğlu, M., Küpçü, R., Demirkesen, C., Şimşek, F., Bağcı, B., Uysal, E., Türker, U., Yıldırım, E., Bayramın, İ., Demirpolat, C., **Kalkan, K.,** 2016. Akıllı Tarım Fizibilite Projesi: Hassas Tarım Uygulamaları için Havadan ve Yerden Veri Toplanması, İşlenmesi ve Analizi. *VI. Uzaktan Algılama ve Coğrafi Bilgi Sistemleri Sempozyumu.*
- Kalkan, B., & **Kalkan, K.,** 2016. Lojistik Yönetiminde Coğrafi Bilgi Sistemi Uygulamaları. *VI. Uzaktan Algılama ve Coğrafi Bilgi Sistemleri Sempozyumu.*

